

RESEARCH ARTICLE

10.1029/2018JB015907

Key Points:

- Analysis of nine heat flux profiles across subduction zones gives apparent coefficients of friction ~ 0.05 – 0.07
- Coefficients for 82 other profiles are 0.07 ± 0.01 , consistent with shear stresses limited by thermal pressurization in earthquakes
- Similarity of friction in all zones implies that zones of historically low seismic moment rate may be capable of generating great earthquakes

Supporting Information:

- Supporting Information S1

Correspondence to:

P. England,
philip.england@earth.ox.ac.uk

Citation:

England, P. (2018). On shear stresses, temperatures, and the maximum magnitudes of earthquakes at convergent plate boundaries. *Journal of Geophysical Research: Solid Earth*, 123, 7165–7202. <https://doi.org/10.1029/2018JB015907>

Received 4 APR 2018

Accepted 27 JUN 2018

Accepted article online 5 JUL 2018

Published online 31 AUG 2018

On Shear Stresses, Temperatures, and the Maximum Magnitudes of Earthquakes at Convergent Plate Boundaries

Philip England¹ 
¹Department of Earth Sciences, University of Oxford, Oxford, UK

Abstract Apparent coefficients of friction, μ' , on nine subduction interfaces for which surface heat flux constraints exist fall in the range $0.05 \lesssim \mu' \lesssim 0.07$. Surface heat flux above the maximum depth of thrust-faulting earthquakes adjusted for radiogenic heat production, Q_T , falls in a narrow range, implying that the transition from seismic to aseismic slip on the interface takes place at a temperature, T_T , that depends upon its depth, z_T . For the mean value of $Q_T \sim 40$ mW/m², $T_T \sim z_T \times 12^\circ\text{C/km}$. The maximum depth of thrust-faulting earthquakes, determined from a further 82 profiles of seismicity across subduction zones, exhibits a systematic dependence on convergence rate and the age of the descending plate, which is consistent with a narrow range in Q_T for these zones also. An analytical expression links μ' to z_T , Q_T , and the subduction parameters. Application of this relation to the 82 profiles gives $\mu' = 0.07 \pm 0.01$. The narrowness of that range can be explained if the primary source of heat on the subduction interface is frictional heating during earthquakes with shear stresses limited by thermal pressurization of pore fluids. Apparent coefficients of friction exhibit insignificant variation with the fraction of the relative motion that is expressed in earthquakes. Either the apparent coefficients of friction for seismic and aseismic slip are indistinguishable or zones with historically low rates of seismicity are prone to large earthquakes that have not been recorded.

1. Introduction

Shear stresses on convergent plate boundaries provide resistance to plate motion and mantle convection, contribute to the support of topography above subduction zones, and influence processes such as metamorphism, dehydration, and melting that are important contributors to the global cycles of rocks and volatiles. It has been suggested that the strength of plate boundaries may control the magnitudes of earthquakes, with some authors attributing the largest earthquakes to plate boundaries with highest shear stresses (e.g., Hardebeck & Loveless, 2017; Scholz & Campos, 2012, 1995), while others contend that the reverse is the case (e.g., Gao & Wang, 2014; Wang & Bilek, 2011, 2014) or that the maximum magnitude is determined by variability, or lack thereof, in the magnitude of stress along subduction zones (e.g., Bletery et al., 2016, 2017; Schellart & Rawlinson, 2013; Wang & Bilek, 2011). The role of dissipative heating in metamorphism and melting at subduction zones is equally contentious; some authors regard dissipation as playing a negligible role (e.g., Abers et al., 2017; Syracuse et al., 2010), while others argue that shear stresses of order 10–100 MPa are required to explain the observations (e.g., England et al., 1992; Graham & England, 1975; Molnar & England, 1990; Peacock, 1992; Penniston-Dorland et al., 2015; Turcotte & Schubert, 1973). Estimates of the stresses required to support topographic slopes above the interface are consistent with coefficients of friction in the range 0.02 to 0.2 (e.g., Barr & Dahlen, 1989; Cattin et al., 1997; Cubas et al., 2013; Dahlen, 1990; Davis et al., 1983; Dielforder, 2017; Lamb, 2006; Suppe, 2007).

Although a few measurements of shear stress have been made in the shallow parts of convergent plate boundaries (e.g., Fulton et al., 2013; Kano et al., 2006; Tanaka et al., 2006), direct measurement are not available at the typical nucleation depths of large and great earthquakes. Indirect estimates of shear stress from heat flux observations have varied from negligible (e.g., Hyndman & Wang, 1993; Hyndman et al., 1995; Wang, Hyndman, et al., 1995; Wang, Mulder, et al., 1995) to ~ 10 –100 MPa (e.g., Fagereng & Ellis, 2009; Gao & Wang, 2014; Von Herzen et al., 2001; Wada & Wang, 2009), and it has been difficult to assess the significance of the differences among these estimates. The ranges in shear stress estimated by different authors for the same subduction zone are comparable with the range of estimates between different subduction zones.

For example, estimates of the apparent coefficient of friction for the Hikurangi margin range from ~ 0.02 (converted from the estimate of shear stress of 20 MPa by McCaffrey et al., 2008), to 0.12 (Gao & Wang, 2014), to >0.3 (Fagereng & Ellis, 2009), while estimates for the Nankai subduction zone vary from 0.03 (Gao & Wang, 2014), to 0.05 (Yoshioka et al., 2013), to $\lesssim 0.1$ (Hamamoto et al., 2011). In comparison, the range in apparent coefficients of friction inferred by Gao and Wang (2014) for 10 different subduction zones is 0.02 to 0.12.

Most previous estimates of shear stress have been made via numerical models, which commonly are tuned to the complexities of individual subduction zones. Those complexities, however, make exploration of the full parameter space unwieldy, and uncertainties are usually not calculated. Gao and Wang (2014, supporting information) write of this difficulty: “It is neither simple nor meaningful to design statistical measures of model fit to the heat flow data. Thus, as in all other thermal modeling efforts, the choice of preferred models is based on visual inspection of results, influenced by the authors’ understanding of the physical process and of the limits of the theoretical model used.” The obstacles to estimating uncertainty in numerical modeling motivates the use, here, of a simple model that yields analytical expressions; these give a transparent view of the relationships between observable quantities—surface heat flux and maximum depth of thrust-faulting earthquakes—and the states of deviatoric stress and temperature at convergent plate boundaries.

2. Physical Model

The analysis is confined to the region in which the two plates are in contact. The interface between the plates is treated as a plane of dip δ across which convergence takes place at a rate V , whose component in the dip direction is V_n (Figure 1; notation is given in Table A1). There are three supplies of heat to the upper plate: heat flux through the top of the lower plate, dissipative heating on the interface between the plates, and radioactive heating in the upper plate. In all the cases considered here the lower plate consists of oceanic lithosphere, within which radiogenic heating may be neglected; heat production within the upper plate is taken to be at a constant rate per unit volume, A , from the surface to a depth D (here taken to be 15 km), and to be zero below that level.

The rate of heating per unit area on the plate interface is given by the product of the apparent shear stress, τ' , and the time-averaged rate of relative motion, V , across the interface. The adjective *apparent* is used here because the relevant shear stress is that during slip on the interface, which may differ greatly from the static shear stress. Slip on subduction interfaces involves a combination of seismic and aseismic processes (e.g., Lay et al., 2012, Figure 15), many of which are thought to be sensitive to confining stress. It is therefore useful to define a parameter

$$\mu' = \frac{\tau'}{\bar{\rho}gz_f}, \quad (1)$$

where g is the acceleration due to gravity and $\bar{\rho}$ is the average density of the rocks overlying the plate interface at depth z_f . The parameter μ' is often referred to as the apparent coefficient of friction, but, as with the apparent stress, μ' is not directly related to any actual coefficient of friction that might be measured for the rocks making up the interface. The term is, however, embedded in the literature of the thermal structure of subduction zones and will be retained here. It should be borne in mind that μ' relates solely to the dissipation of energy in heat during slip, regardless of the mechanism by which slip takes place. In comparing μ' with actual coefficients of friction the simplifying assumption will be made that the normal traction on the gently dipping subduction interface may be approximated by $\bar{\rho}gz_f$; this is reasonable because shear stresses are very small in comparison with confining pressures.

2.1. Analytical Expressions Relating Surface Heat Flux to Temperature and Shear Stress

Over the depth ranges in which the two plates are in contact, temperatures are determined by thermal diffusion perpendicular to the plate interface and advection of heat by the relative motion of the plates parallel to the interface; diffusion parallel to the plate interface is negligible. Approximate analytical expressions for temperatures (Molnar & England, 1990, 1995; Tichelaar & Ruff, 1993) are extended in Appendix A to take account of the temperature dependence of thermal properties and to give other expressions that are required for the present analysis. Molnar and England (1990) showed that the analytical approximations agree with 2-D numerical solutions at the level of about 1%.

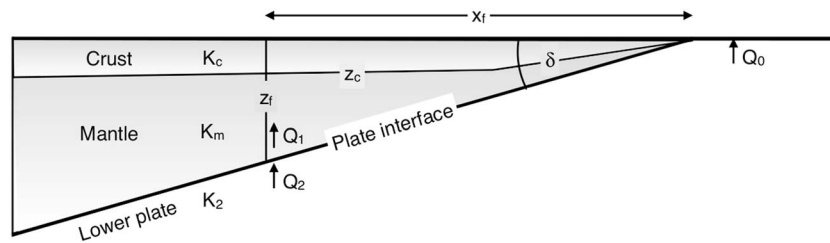


Figure 1. Definition sketch for the physical model of temperatures at convergent plate boundaries. The sketch is drawn perpendicular to the strike of the plate interface, which has dip δ . The lower plate is oceanic in all the cases considered here and has thermal conductivity K_2 . The upper plate consists of mantle, conductivity K_m , and crust, of thickness z_c and conductivity K_c . All conductivities are temperature-dependent (Appendix A). The conductive heat flux through the surface of ocean floor entering the trench is Q_0 ; Q_1 and Q_2 are, respectively, the heat flux into the base of the upper plate, and out of the top of the lower plate. Q_1 is greater than Q_2 , by the rate of frictional heating per unit area on the plate interface, here treated as being infinitesimally thin. z_f is the depth of a point of interest on the plate interface; x_f is the horizontal distance of that point from the trench.

The solutions employed here assume that temperatures are in a steady state, which Molnar and England (1990) showed is approached within a few million years of the onset of subduction. The expressions of Appendix A are given here in their simplified forms, which apply when the depth to the subduction interface, z_f , is greater than the depth range, D , over which heat production, A , is distributed. Under that condition the temperature on the subduction interface is (equation (A9))

$$T_f = \frac{(Q_0 + \tau'V)z_f + AD^2/2}{K_1 S}, \quad (2)$$

where Q_0 is the heat flux through the upper surface of the lower plate immediately before it enters the subduction zone, τ' is the apparent shear stress, V is the long-term average rate of slip across the plate boundary, and K_1 is the appropriately averaged thermal conductivity of the upper plate (Appendix A).

$$S = 1 + \frac{2K_2}{K_1} \sqrt{\frac{z_f V_n \sin \delta}{\pi \kappa}}, \quad (3)$$

where κ is thermal diffusivity, K_2 is the thermal conductivity of the lower plate close to the subduction interface (taken to be the conductivity of the mantle at temperature T_f ; see Appendix A) and V_n is the component of relative velocity in the direction perpendicular to strike of the plate boundary.

Equation (2) shows that temperatures on the plate interface are diminished, by the factor S , below the steady state solution to the 1-D (vertical) diffusion equation that would be obtained if all the same heat sources were present (equation (A11)). The form of S arises from the fact that a boundary layer of thickness $\sim \sqrt{\pi \kappa t}/2$ develops on the top of the lower plate during the time, t , taken for the plate to travel from the trench to the depth z_f (equation (A3)). In consequence, the heat flux into the base of the lower plate is diminished by an amount that represents the heating of the top of the lower plate. See, for example, the discussion of equations (A3)–(A6).

The surface heat flux, Q_s , is related to the heat sources by

$$Q_s = \frac{Q_0 + \tau'V}{S} + AD \left(1 - \frac{D}{2z_f} \left(1 - \frac{1}{S} \right) \right). \quad (4)$$

Equation (4), written in terms of μ' , is used in section 3.1 to estimate apparent stresses on nine subduction interfaces from profiles of heat flux. As seen for temperatures on the fault (equation (2)), only a fraction $1/S$ of the heat sources at or below the fault ($Q_0 + \tau'V$) reaches the surface; in contrast, practically all of the heat generated in the crust, AD , reaches the surface (the term multiplying AD in equation (4) is close to 1 for most cases). For this reason, uncertainties in AD can exert a significant influence on estimates of shear stress, as discussed in section 2.3.

The temperature on the fault can be calculated from the measured surface heat flux, Q_s , and estimated heat production, AD .

$$T_f = \frac{z_f}{K_1} \left[Q_s + AD \left(\frac{D}{2z_f} - 1 \right) \right]. \quad (5)$$

This expression is used, in section 3.2, to determine the temperatures, T_T , at the maximum depths of thrust-faulting earthquakes, z_T , in those zones. It is found that $T_T \propto z_T$, hence that a quantity

$$Q_T = \frac{K_1 T_T}{z_T} \quad (6)$$

is approximately constant across the different zones. The value of Q_T obtained in section 3.2 is used in section 3.3 to estimate apparent shear stresses at z_T on a further 82 profiles for which no heat flux constraint is available. When $z_T \geq D$

$$\tau' = \frac{S Q_T - Q_0 - AD^2/(2z_T)}{V}. \quad (7)$$

In comparison with estimates of τ' from surface heat flux (equation (4)), these estimates are relatively insensitive to uncertainties in AD (section 2.3).

2.2. Uncertainties in Measurements

The measurements used to estimate shear stresses are of the rate of convergence between the plates, of the depth of the plate interface, of surface heat flux above the plate interface, of the age of the ocean floor entering the trench, and, through this, its surface heat flux. One further important quantity, the rate of radiogenic heat production per unit area of upper plate, has to be estimated from sparse measurements of the volumetric rate of heat production in near-surface sediments.

Convergence rates and trench-perpendicular rates, V and V_n , are taken from the NNR-MORVEL56 model of plate motions (Argus et al., 2011). Their uncertainties can be estimated from the root-mean-square (RMS) misfit of GPS velocities to that model, which are ~ 3 mm/year (Argus et al., 2011); these are a few percent of the rates themselves. Estimates of the depth to the plate interface are taken from Slab 1.0 (Hayes et al., 2012) who show that, for the depth range considered here, uncertainties in z_T , which lies in the range ~ 30 – 70 km, are about 5 km, or $\sim 7\%$ to 17% of z_T .

The heat flux, Q_0 , through the upper surface of the lower plate immediately before it enters the subduction zone is assigned using the thermal plate model of Parsons and Sclater (1977):

$$\begin{aligned} Q_0 &= 0.473/\sqrt{a} \text{ W/m}^2 & a < 60 \\ Q_0 &= (0.037 + 0.067 \exp(-a/62.8)) \text{ W/m}^2 & a \geq 60, \end{aligned} \quad (8)$$

where a is age of the ocean floor in million years. (Differences between this model and that of Stein and Stein (1992) are negligible in the present context.) The cooling of the ocean floor by hydrothermal circulation (e.g., Lowell et al., 1995; Stein & Stein, 1994; Wolery & Sleep, 1976) is approximated by multiplying the conductive heat flux (equation (8)) by a factor

$$f = 0.5 + a/134 \quad a \leq 67 \quad (9)$$

(Stein & Stein, 1994, Figure 4).

The measurements of surface heat flux, Q_s , used here are those compiled by Gao and Wang (2014), from sources cited by them. When uncertainties are given in the original sources they are used, except as noted below. An uncertainty of 10 mW/m^2 is assigned to those measurements without published uncertainties on the basis that, in many of the profiles analyzed, heat flux measurements close to one another exhibit scatter at that level (e.g., Figures 2d and 2e). This variability arises from one or more of a number of causes that cannot be diagnosed from the measurements; these probably include variation in bottom water temperature, slumping or deposition of sediment, and advection of heat by fluids circulating within, or expelled from, the accretionary prism. Because of this variability, an uncertainty of 10 mW/m^2 is also assigned to measurements whose published uncertainties are lower than that level. Most of the probable sources of variability could either depress or raise the conductive heat flux measurements, and it is reasonable to treat them as aleatoric sources of error. In the region close to the trench, however, it seems likely that there is significant upward transport of heat by water that expelled in compaction of the sediments (e.g., Hass & Harris, 2016; Saffer & Tobin, 2011; Spinelli & Harris, 2011; Spinelli & Wang, 2009). Surface heat flux measurements are therefore excluded if they lie within 40 km of the trench.

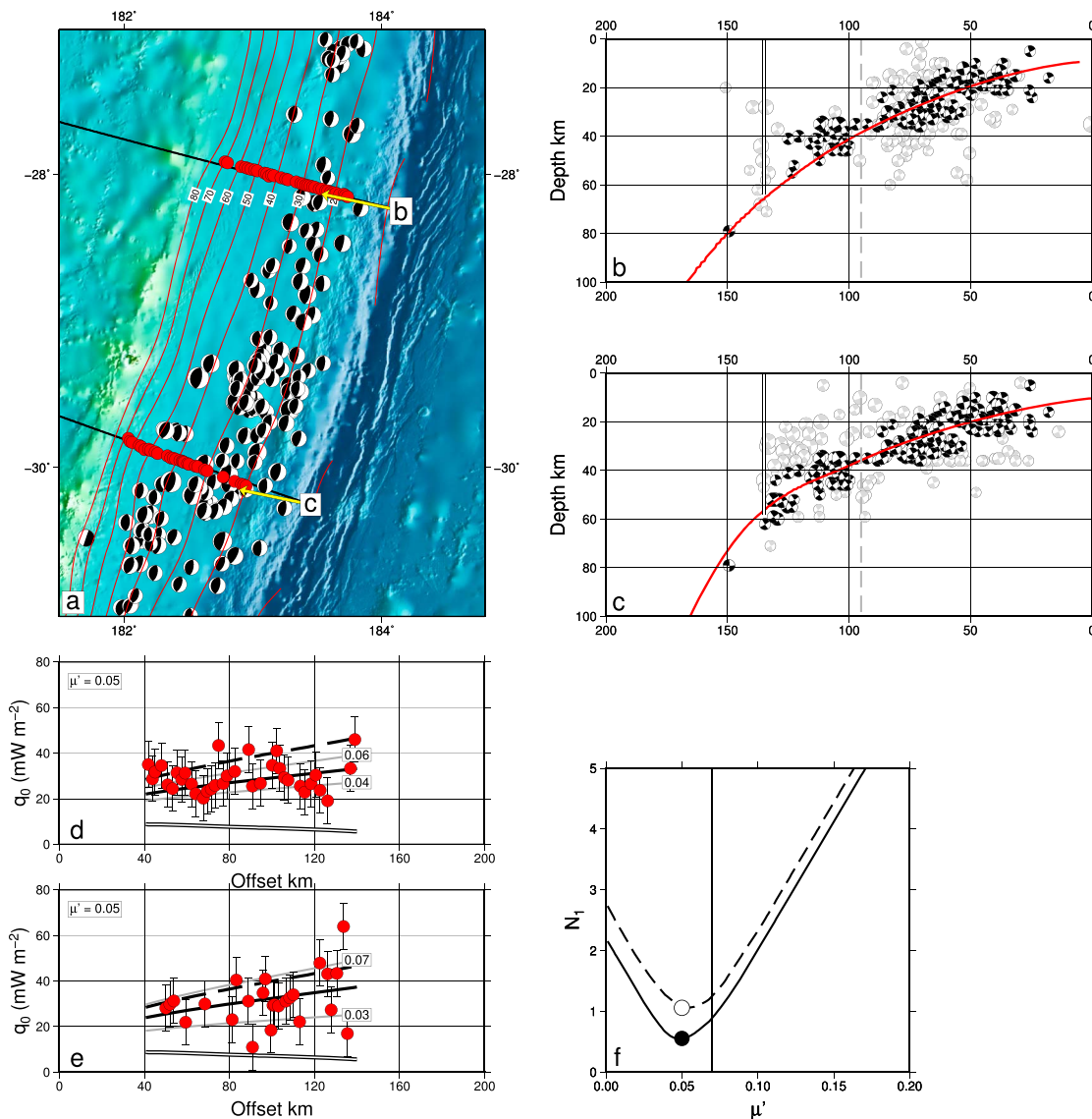


Figure 2. Analysis of heat flux measurements in the Kermadec region (Von Herzen et al., 2001). (a) Map showing distribution of heat flux measurements (red symbols) and focal mechanisms of reverse-faulting earthquakes from the global centroid moment tensor catalog (Dziewonski et al., 1981; Ekström et al., 2012), with hypocenters given by International Seismological Centre (2015). Black lines show profiles for projections of seismicity (b, c) and heat flux (d, e); yellow arrows show direction of motion of Pacific plate relative to the Kermadec plate as defined by MORVEL56 (Argus et al., 2011). Red contours show depth to the top of the slab (Hayes et al., 2012). (b, c) Focal mechanisms are those of thrust-faulting earthquakes within 100 km of profiles b and c in (a); those with black fill are within 10 km of the slab surface as defined by Hayes et al. (2012; red lines). Mechanisms are plotted as though viewed looking into the page. Double vertical line shows horizontal location of maximum depth of thrust-faulting earthquakes. Vertical dashed lines show the horizontal coordinate of the peak stress on the subduction interface, read from the relevant figure of Gao and Wang (2014); this is taken to be the transition between frictional and viscous behavior on the interface in their model. (d, e) Red symbols show heat flux measurements. Black line shows heat flux predicted by best fitting model with a constant apparent coefficient of friction on the interface (equation (A14)); μ' given in box at top left. Dashed line shows the fit with the value of μ' chosen by Gao and Wang (2014). Grey lines show fits with the upper and low values of μ' , obtained from uncertainties in heat flux as described in the text. Double line is calculated for $\mu' = 0$. (f) Variation with μ' of weighted misfits to heat flux observations (N_1 , equation (16)). Solid line with symbol at minimum: heat flux measurements from northern profile (b, e). Dashed line with open symbol: measurements from the southern profile (c, f). Vertical line shows the value of μ' chosen by Gao and Wang (2014).

The largest uncertainties are associated with estimates of radiogenic heat production within the upper plate. Gao and Wang (2014) compiled measurements of the rate of heat production, A , from near-surface rocks in some of the subduction zones and, where such measurements were absent, used representative values for continental, fore-arc, or ocean-floor sediments, assuming that the heat production is mainly in an upper crust of thickness $D = 15$ km. Similar approaches are adopted in other studies (e.g., Oleskevich et al., 1999; Syracuse et al., 2010; Wada & Wang, 2009). This approach carries a significant epistemic uncertainty.

The common assumption that radiogenic heating is concentrated in the upper crust is based on a small number of studies of heat flux in continental interiors (e.g., Birch et al., 1968; Blackwell, 1971; Jaupart & Mareschal, 2011; Sclater et al., 1981; see also Furlong & Chapman, 1987). There is no evidence that such a length scale is appropriate for the distribution of heat production within sediments at subduction boundaries. The present analysis uses Gao and Wang (2014) estimates of AD , but they are taken to be uncertain by $\pm 50\%$, which may be an underestimate.

2.3. Uncertainties in Analysis

In section 3.1 apparent coefficients of friction are estimated from heat flux profiles using equation (A14), which reduces to equation (4) for $z_T > D$. Uncertainties in the analysis may be understood by rearranging equation (4) to give an approximate form that is valid when $D \ll 2z_T$. That condition that is met in most of the cases considered here, where $z_T \gtrsim 30$ km, and it is assumed that $D \sim 15$ km.

$$\mu' \sim \frac{S(Q_s - AD) - Q_0}{\bar{\rho}gz_T V}, \quad (10)$$

Equation (10) contains quantities whose uncertainties are low (V , $\bar{\rho}g$), heat fluxes, and the term S/z_T , uncertainties in which are clarified by writing

$$S \sim 1 + \frac{2z_T K_2}{K_1} \sqrt{\frac{V_n}{\pi \kappa x_T}} \quad (11)$$

$$\frac{S}{z_T} \sim \frac{2K_2}{K_1} \sqrt{\frac{V_n}{\pi \kappa x_T}} \quad (\text{when } S \gg 1), \quad (12)$$

where x_T is the horizontal location immediately above the maximum depth of thrust-faulting earthquakes, z_T . Fractional uncertainties in x_T are of the order of a few percent (Appendix C), as are those in V_n . The remaining uncertainty in S/z_T arises from the thermal diffusivity, κ , and K_2/K_1 , the ratio of the thermal conductivity near the top of the lower plate to the average conductivity of the upper plate. The relevant thermal diffusivity is that of the uppermost part of the lower plate at temperatures, which, it will be seen, are generally between about 400°C and 700°C (Figure 6a). To within 20%, that diffusivity may be approximated by a constant value of 10^{-6} m²/s (Figures A1a and A1b). Although, for the relevant temperature ranges, K_1 and K_2 vary separately by over 50%; their ratio lies in the range $0.9 < K_1/K_2 < 1.1$ for nearly all of the relevant temperature range (Figure A1). From these considerations, a reasonable estimate for the fractional uncertainties in S/z_T is 10–15%.

Differentiating equation (10) with respect to the heat flux terms, Q_s , AD , and Q_0 gives

$$\frac{\partial \mu'}{\partial Q_s} = -\frac{\partial \mu'}{\partial (AD)} \sim \frac{S}{V \bar{\rho}gz_T} \sim \frac{1}{\bar{\rho}g} \sqrt{\frac{\sin \delta}{V z_T \kappa}} \quad \text{for } S \gg 1, \quad (13)$$

$$\frac{\partial \mu'}{\partial Q_0} \sim -\frac{1}{V \bar{\rho}gz_T}. \quad (14)$$

Uncertainties in Q_s are at least 10 mW/m² (Figures 2–4 and B1–B5). For $V \sim 80$ mm/year, $z_T \sim 50$ km, and $\bar{\rho} \sim 3,000$ kg/m³, an uncertainty of 10 mW/m² in Q_s translates into an uncertainty of 0.015 in μ' . Uncertainties in AD range from negligible, in the case of the Kermadec subduction zone, to ~ 20 mW/m² in the cases of Japan and the Hikurangi margin, which translates into an uncertainty of 0.03 in μ' . A comparable uncertainty is associated with departures from the assumption that $D \sim 15$ km. If D were 30 km, then, for a given AD , μ' would be higher by 0.01 to 0.03, except for the Kermadec profile.

The sensitivity of estimates of μ' to uncertainties in Q_0 is smaller than to Q_s or AD by the factor S (equation (10)), which lies in the range 4–12 (Table 1). However, as will be discussed for the Cascadia and Nankai subduction zones (Figures 4 and B2), where the lower plate consists of ocean floor younger than ~ 20 Myr, the uncertainty in Q_0 may exceed 30 mW/m². For ocean floor older than about 50 Myr, the influence of the hydrothermal adjustment becomes smaller than 10 mW/m², comparable with uncertainties in measurement of Q_0 . Combining the sources of uncertainty, we should expect uncertainties in the apparent coefficient of friction estimated from surface heat flux to be around 0.05, and higher in subduction zones containing young ocean floor.

In section 3.3 apparent coefficients of friction are estimated from the maximum depth of thrust-faulting earthquakes using equation (A19). Q_T is, effectively, the difference between the surface heat flux at the maximum

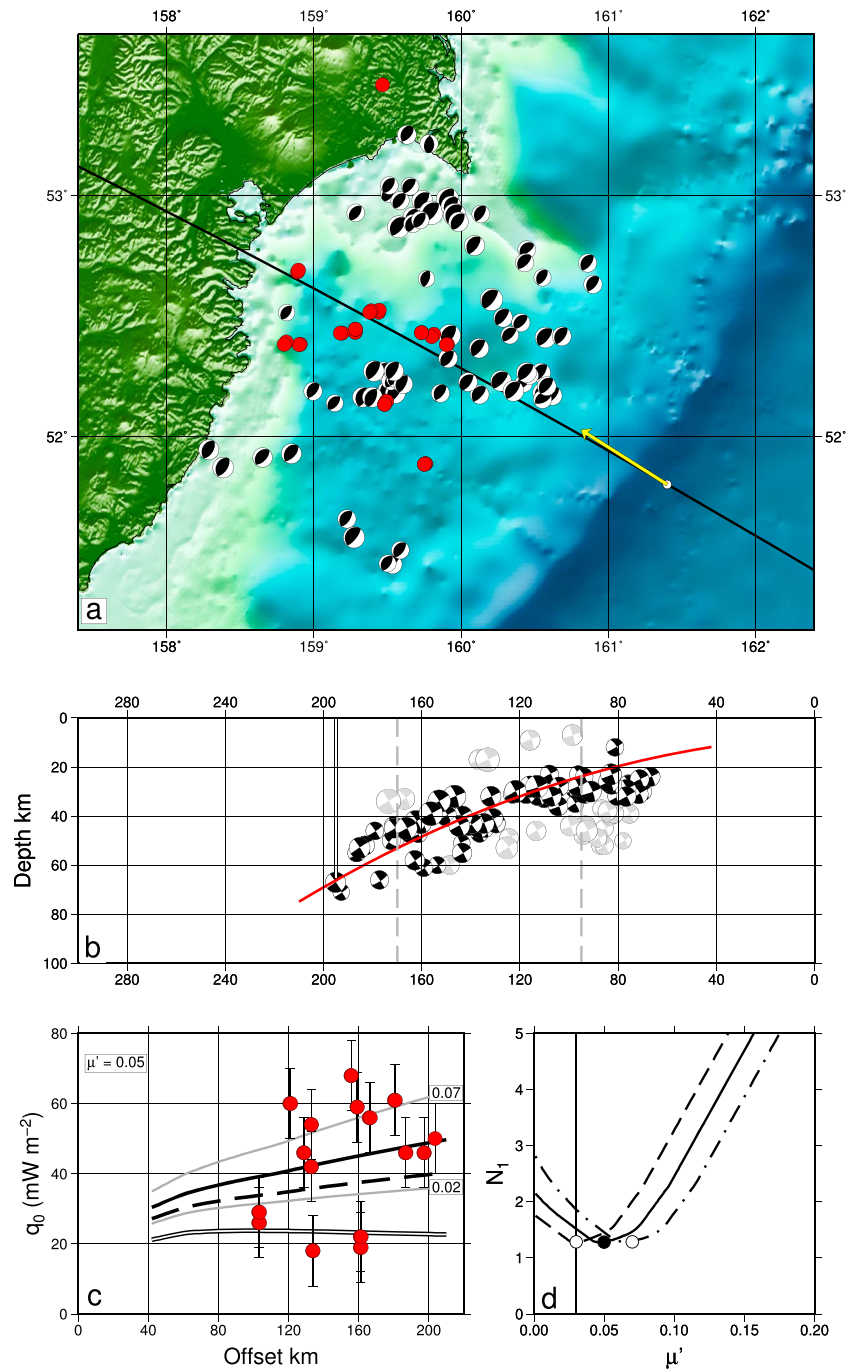


Figure 3. As in Figure 2 but for Kamchatka. In panel (d), the dashed and dash-dotted lines show the variation in weighted misfit (N_1 , equation (16)) calculated with AD , respectively, at 1.5 and 0.5 times the value of 19.5 mW/m^2 adopted by Gao and Wang (2014).

depth of thrust faulting, z_T , and the total heat radiogenic production above that depth (equation (A18)). Although uncertainties in AD affect the estimates of Q_T , once the uncertainty Q_T is determined (section 3.1) further uncertainty due to AD is small because the term SQ_T is large in comparison with AD (see equations (7) and (A20)). From equation (A20)

$$\frac{1}{\mu'} \frac{\partial \mu'}{\partial Q_T} = \frac{1}{Q_T}. \quad (15)$$

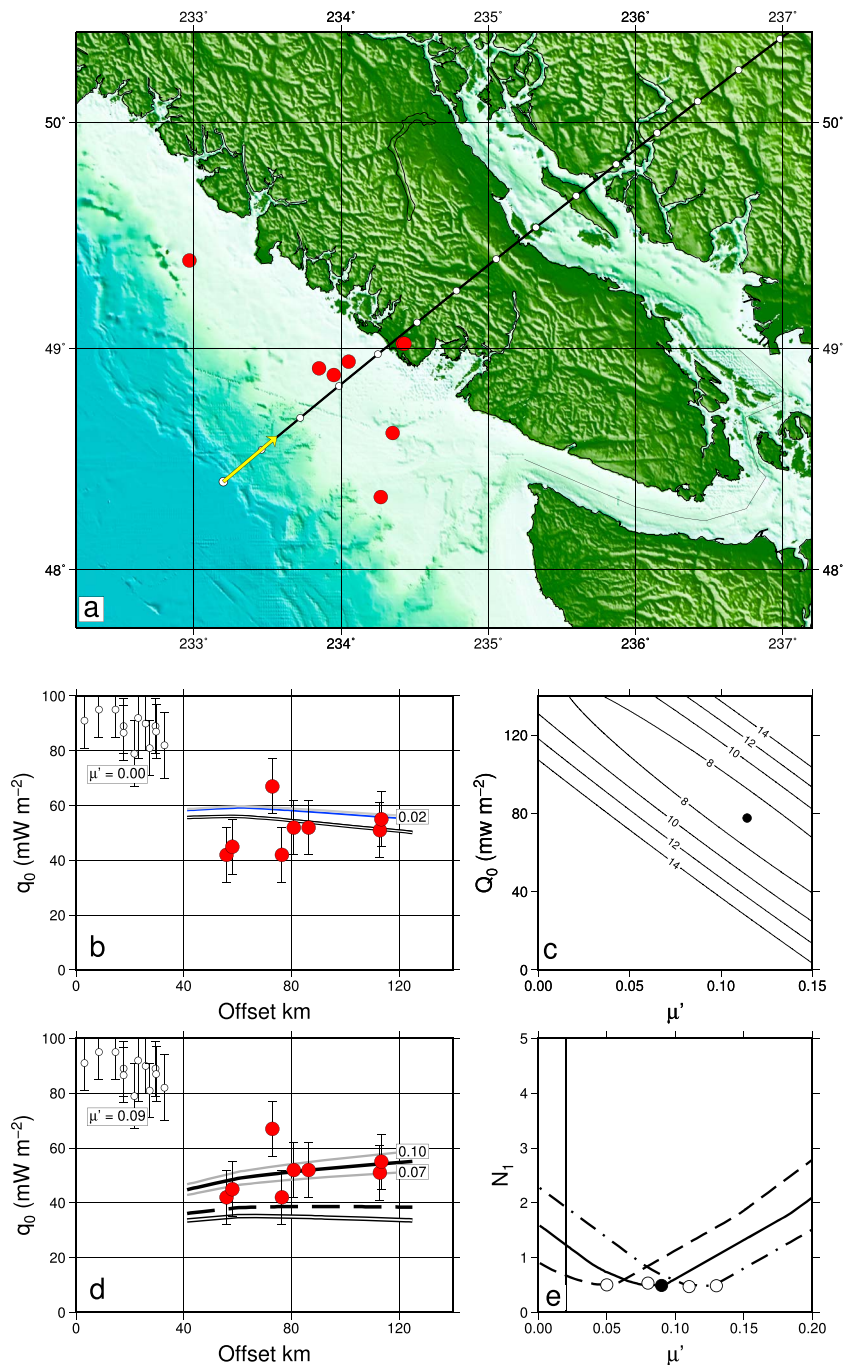


Figure 4. Estimates of μ' for the northern Cascadia margin. Symbols as in Figure 3 except as mentioned here. (b) The solution obtained with Q_0 fixed to 140 mW/m^2 , the value for ocean floor of age 11 Myr from the thermal plate model (equation (8)); open symbols show heat flux measurements less than 40 km from the trench (see section 2.2). (c) Contours of mean misfits to heat flux observations as Q_0 and μ' are varied. Black dot shows the location of minimum misfit. (d) Solutions for μ' with Q_0 fixed to 80 mW/m^2 (minimum misfit in panel c). In panel (e), the dashed and dash-dotted lines show the variation in weighted misfit (N_1 , equation (16)) calculated with AD , respectively, at 1.5 and 0.5 times the value of 19.5 mW/m^2 adopted by Gao and Wang (2014).

3. Estimates of Shear Stresses and Temperatures on Subduction Interfaces

3.1. Estimation of Apparent Coefficient of Friction From Surface Heat Flux Profiles

This section obtains estimates of the apparent coefficient of friction from nine profiles of heat flux above the seismogenic portions of convergent plate boundaries, previously analyzed by Gao and Wang (2014). In their

Table 1
Average Values of Parameters of Subduction Zone Segments

Name	Longitude (°E)	Latitude (°N)	z_T^a (km)	x_T^a (km)	W^b (km)	δ^c (°)	v^d (mm/year)	V_n^d (mm/year)	S	Age (Myr)	τ (MPa)	μ'	χ^e	M_x^f
Honshu	143.6	37.9	63	229	200	15	92	92	8.9	129	106	0.056	0.59	9.0
Hokkaido	146.2	41.8	64	197	175	18	91	80	9.0	128	108	0.057	0.66	8.5
S Kuriles	151.0	44.4	50	143	121	19	89	80	8.3	116	100	0.063	0.59	8.5
N Kuriles	156.3	48.0	50	147	125	18	86	84	8.5	110	106	0.066	0.59	8.5
Kamchatka	162.0	52.8	61	168	150	20	82	82	9.4	102	123	0.067	0.51	8.9
W Aleutians	175.0	51.1	46	115	96	22	76	33	5.8	49	72	0.049	0.82	8.7
C Aleutians	−173.0	51.0	56	146	129	21	71	63	8.3	56	119	0.066	0.82	8.6
E Aleutians	−162.0	53.2	51	153	129	18	66	64	7.5	55	114	0.071	0.70	9.1
Alaska	−153.0	55.6	29	162	107	10	61	61	4.5	47	62	0.078	0.60	9.3
Mexico	−101.0	16.7	32	108	78	16	64	64	5.9	7	66	0.072	1.00	8.1
C America	−89.6	11.9	58	124	114	25	76	75	9.6	23	131	0.077	0.10	7.6
N Peru	−81.6	−7.0	27	120	77	13	66	65	4.9	29	62	0.084	0.02	8.5
C Peru	−74.2	−17.0	47	143	118	18	71	62	7.1	48	98	0.072	0.75	9.2
N Chile	−71.3	−22.0	58	162	142	19	73	70	8.4	52	120	0.070	0.75	9.1
C Chile	−72.5	−30.4	51	143	122	19	73	66	7.8	41	106	0.071	1.00	8.8
S Chile	−74.6	−37.0	39	150	115	15	74	65	6.1	32	76	0.068	1.00	9.6
Scotia	−24.2	−58.0	49	116	100	23	73	64	8.1	44	114	0.072	—	7.0
N Sumatra	95.8	1.0	60	223	193	15	53	45	6.4	53	113	0.063	0.70	9.3
S Sumatra	101.0	−5.5	70	244	218	16	58	53	7.5	79	131	0.062	0.70	9.2
Java	105.5	−8.8	63	225	196	16	64	62	7.5	103	122	0.065	0.01	7.7
Philippines	127.1	9.0	63	87	90	36	102	83	12.1	50	131	0.069	—	—
Ryukyu	130.2	27.2	56	175	151	17	65	63	7.7	52	119	0.067	0.00	8.0
Izu-Bonin	142.1	33.0	49	112	97	24	47	47	7.1	135	161	0.103	0.01	7.2
Mariana	147.7	18.6	56	130	116	23	52	52	7.8	147	164	0.092	0.01	7.2
Solomons	155.0	−7.3	55	95	89	29	101	80	10.3	17	101	0.059	0.13	—
Vanuatu	168.4	−20.0	52	78	76	33	116	107	12.2	32	116	0.070	0.13	7.8
Tonga	−173.6	−20.9	40	111	88	19	155	152	9.8	91	76	0.060	0.45	8.3
Kermadec	183.4	−30.0	59	126	116	25	97	97	10.9	97	127	0.067	0.18	8.1

^aMaximum depth, z_T , of thrust-faulting earthquakes, and its horizontal distance from trench, x_T . Details for each profile in the segment are given in the supporting information. ^bDowndip distance along slab from depth of 10 km to z_T . ^cAverage dip of slab to depth z_T : $\arctan(z_T/x_T)$. ^dFrom Argus et al. (2011). ^eFraction of plate relative motion accommodated by earthquakes, from Scholz and Campos (1995, 2012). ^fRecorded maximum magnitude of earthquakes, from Stein and Okal (2007), updated by Hayes et al. (2012).

numerical models Gao and Wang (2014) specify the shear stress by a combination of frictional sliding and viscous dissipation in a shear zone whose rheology is that of wet granite, with the transition between the two mechanisms being determined by the temperature and stress on the interface. A consequence of this choice of rheology is that the depth of transition from seismic to aseismic behavior along the interface depends upon the choice of μ' . In the one case where they illustrate this effect (Gao & Wang, 2014, supporting information Figure S4) the transition depth varies between ~ 30 km for $\mu' = 0.03$ and ~ 60 km for $\mu' = 0.09$ (see Figure 3). In the present analysis, the location of the transition between seismic and aseismic behavior is taken from seismic observations (Appendix C) and the apparent coefficient of friction is determined for the depth range over which the interface exhibits thrust-faulting earthquakes.

For each profile of surface heat flux (Figures 2–4 and B1–B5), the best fitting value of the apparent coefficient of friction, μ' , is found from the minimum in the mean weighted misfit

$$N_1 = \frac{1}{n} \sum_{i=1}^n \left| \frac{Q_i - q_i}{\sigma_i} \right|, \quad (16)$$

where Q_i and q_i are the observed heat fluxes and those predicted by equation (A14), with the weights, σ_i , being the uncertainties in, and n the number of, the observations. The discussion of section 2.3 shows that the

principal uncertainties in μ' arise from uncertainty in the difference between Q_s and AD , and from whether a hydrothermal adjustment should be applied to Q_0 (equation (9)). The range in μ' due to uncertainties in Q_s alone is calculated for each profile by multiplying the minimum in N_1 by the term $S/(V\bar{\rho}gz_T)$ (equation (13)), evaluated at the maximum depth of thrust-faulting earthquakes for that profile. This aspect of the procedure is illustrated in Figure 2 for heat flux profiles measured across the Kermadec subduction zone by Von Herzen et al. (2001), which are the only profiles for which radiogenic heating is negligible. For the remaining profiles, uncertainties in AD are up to 20 mW/m²; uncertainties in μ' from this source are estimated by calculating μ' with AD at the value assumed by Gao and Wang (2014) and at 0.5 and 1.5 times that value. The range of μ' so obtained is taken as the uncertainty due to uncertainties in AD alone. This aspect of the procedure is illustrated in Figures 3 and B1–B5. Uncertainties associated with the heat flux through young ocean floor (equation (9)) are investigated for the Cascadia and Nankai subduction zones in Figures 4 and B2.

3.1.1. Kermadec

The northern and southern profiles of heat flux across the Kermadec trench (Von Herzen et al., 2001) are best fit, respectively, by $\mu' \sim 0.05$ ($0.04 < \mu' < 0.06$) and $\mu' = 0.05$ ($0.03 < \mu' < 0.07$) (Figures 2d and 2e). These ranges in μ' are consistent, as discussed in section 2.3, with uncertainty of 10 mW/m² in Q_s . Von Herzen et al. (2001) used the analytical expressions of Molnar and England (1990) and concluded that the heat flux observations are satisfied either by a constant shear stress of $\sim 40 \pm 17$ MPa or by a linearly increasing shear stress equivalent to $\mu' \sim 0.06 \pm 0.03$. Gao and Wang (2014, supporting information Figure S2) obtained a value for μ' of 0.07 from their numerical model. They concluded that the measurements may be fit by apparent coefficients of friction in the range $0.04 \lesssim \mu' \lesssim 0.1$, comparable with the range obtained in the present analysis (Figure 2).

3.1.2. Kamchatka

The procedure for the remaining profiles, in which there are also uncertainties in AD , is illustrated in Figure 3 for the profile across Kamchatka, for which AD is taken to be 19.5 mW/m² (Gao & Wang, 2014, supporting information Figure S4). Gao and Wang (2014) argued that the heat flux observations cannot be fit with $\mu' > 0.09$ and chose a value of 0.03. The present analysis yields a best fitting value of $\mu' = 0.05$ ($0.02 < \mu' < 0.07$), or $0.03 \lesssim \mu' \lesssim 0.07$ if uncertainties in heat production alone are considered.

3.1.3. Cascadia

The maximum depth of thrust faulting cannot be determined for this profile because of the paucity of focal mechanisms. Instead it is assumed to coincide with the line of 20% locking, as determined by Schmalzle et al. (2014). That line follows closely the updip limit of slow-slip events (Wech & Creager, 2011) and the 30-km contour of depth of the slab, and is about 120 km from the trench. The line of the profile is the same as that of Gao and Wang (2014), but those authors modeled heat flux out to 240 km from the trench, at which distance the top of the slab is deeper than 50 km.

The age of the ocean floor beneath this region is approximately 10–12 Myr (Wilson, 1993, 2002). Using the thermal plate model (equation (8)) to estimate Q_0 for this age yields a best fitting value of $\mu' = 0.0$ ($0 < \mu' < 0.02$; Figure 4b). Hutnak et al. (2006) argued that there is significant (perhaps 20% regionally) hydrothermal heat transfer through places where basement is exposed. Furthermore, Phrampus et al. (2017) show that the heat flux inferred from bottom-simulating reflectors along their Profile A (close to the profile of Figure 4) is consistently lower than would be predicted for a purely conductive lower plate (see also Cozzens & Spinelli, 2012). The maximum heat flux near the deformation front is about 120 mW/m² (Phrampus et al., 2017).

Figure 4c displays the mean misfits to the heat flux values (calculated using equation (16) with unit weights) that are obtained by systematically varying Q_0 between zero and 140 mW/m² and finding the best fitting value of μ' corresponding to each value of Q_0 . The lowest misfit is found with $Q_0 = 80$ mW/m² and $\mu' = 0.11$, but this is not to be regarded as a rigorous estimate. The principal feature of Figure 4c is the sensitivity of the estimates of μ' to uncertainty in Q_0 . If, for example, Q_0 is allowed to vary between 140 and 80 mW/m² (the values for a lower plate of age 12 Myr without and with hydrothermal adjustment: equations (8) and (9)), then solutions within the contour representing a mean misfit of 8 mW/m² (less than 15% above the minimum of 7.1 mW/m²) allow $0 \lesssim \mu' \lesssim 0.14$ (Figure 4c). If Q_0 is set at 80 mW/m², then $0.07 < \mu' < 0.1$ (Figure 4d) and the uncertainty in μ' arising from assumptions about heat production is $\sim \pm 0.04$ (Figure 4e).

Many studies of this subduction zone using numerical models have concluded that shear heating on the interface is small or negligible (e.g., Hyndman & Wang, 1993; Wang, Mulder, et al., 1995; Wada & Wang, 2009);

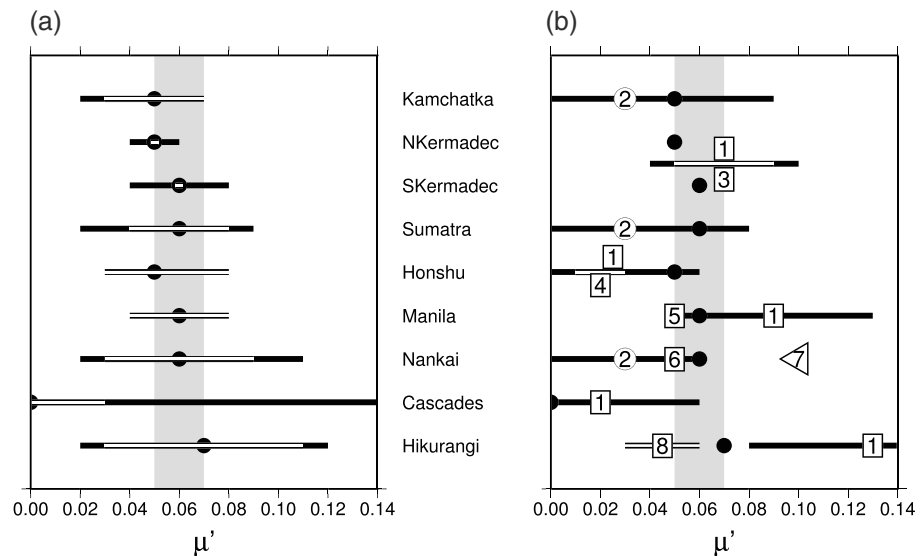


Figure 5. Estimates of the apparent coefficient of friction on subduction interfaces from profiles of surface heat flux. (a) Solid symbols show best fitting values of μ' as determined in Figures 2–4 and B3–B5 (equation (A16)). Solid lines show ranges in estimates of μ' arising from uncertainties in surface heat flux measurements; double lines show ranges associated with uncertainty in heat production (section 2.3). Grey shading corresponds to $0.05 < \mu' < 0.07$. (b) Comparison with estimates of μ' reported in other studies. Solid symbols as in (a); numbers within open symbols refer to studies as follows: (1) Gao and Wang (2014), solid lines correspond to their chosen ranges of μ' ; (2) values assumed by Wada and Wang (2009) and accepted by Gao and Wang (2014); (3) estimate of Von Herzen et al. (2001), with its uncertainty shown by white line; (4) Furukawa and Uyeda (1989), with its uncertainty shown by white line; (5) Chi and Reed (2008), as discussed in section B3; (6) Yoshioka et al. (2013); (7) upper bound of Hamamoto et al. (2011); (8) McCaffrey et al. (2008), as discussed in section B1.

Gao and Wang (2014) choose a value of 0.02. The analysis of this section suggests that it is not possible to use heat flux to estimate μ' for this profile with any confidence.

3.1.4. Other Profiles

The procedures described here are applied to five further profiles in Appendix B (Figures B1–B5). Best fitting values of μ' for all nine profiles lie, with the exception of the Cascadia profile for which μ' is indeterminate, in the range $0.05 \lesssim \mu' \lesssim 0.07$ (Figure 5a). With the exception of the two subduction zones containing young ocean floor (Cascadia, Figure 4, and Nankai, Figure B2) the heat flux observations rule out a coefficient of friction of zero (Figures 2, 3, B1, and B3–B5). The range in estimates of μ' in previous studies is 0 to 0.13, although the uncertainties in those estimates are mostly unknown. Apart from the estimates of $\mu' \sim 0.025$ by Furukawa and Uyeda (1989) and Gao and Wang (2014) for the Honshu profile and the estimate of Gao and Wang (2014) for the Hikurangi margin, previous estimates fall within the uncertainties determined in this analysis (Figure 5b). It seems probable that some of the differences between the present study and that of Gao and Wang (2014) arise from different treatments of uncertainties, and from the latter's entwined relation between the model rheology and the maximum depth of thrust faulting on the interface.

The range in estimates of μ' obtained here is comparable with the range to be expected from uncertainties in heat flux and heat production (section 2.3), so we cannot reject the hypothesis that the apparent coefficient of friction is constant across the subduction zones for which heat flux profiles exist. Such a conclusion would apply, however, only to a restricted range of the world's subduction zones. In order to sample a larger range of subduction zones, it is necessary to introduce a proxy for heat flux, which is derived in section 3.3 from the maximum depth of thrust-faulting earthquakes.

3.2. Temperatures at Maximum Depth of Thrust-Faulting Earthquakes

The surface heat flux observations may be used to estimate temperatures on the plate interface. It is of particular interest to determine the temperature at the transition from seismic to aseismic slip, commonly taken to be the transition between velocity-weakening and velocity-strengthening friction (e.g., Scholz, 1998). The maximum depth of thrust-faulting earthquakes, z_T , is determined for each of the heat flux profiles, as described in Appendix C. Temperatures, T_T , at those depths are calculated from equation (A17) with a nominal value

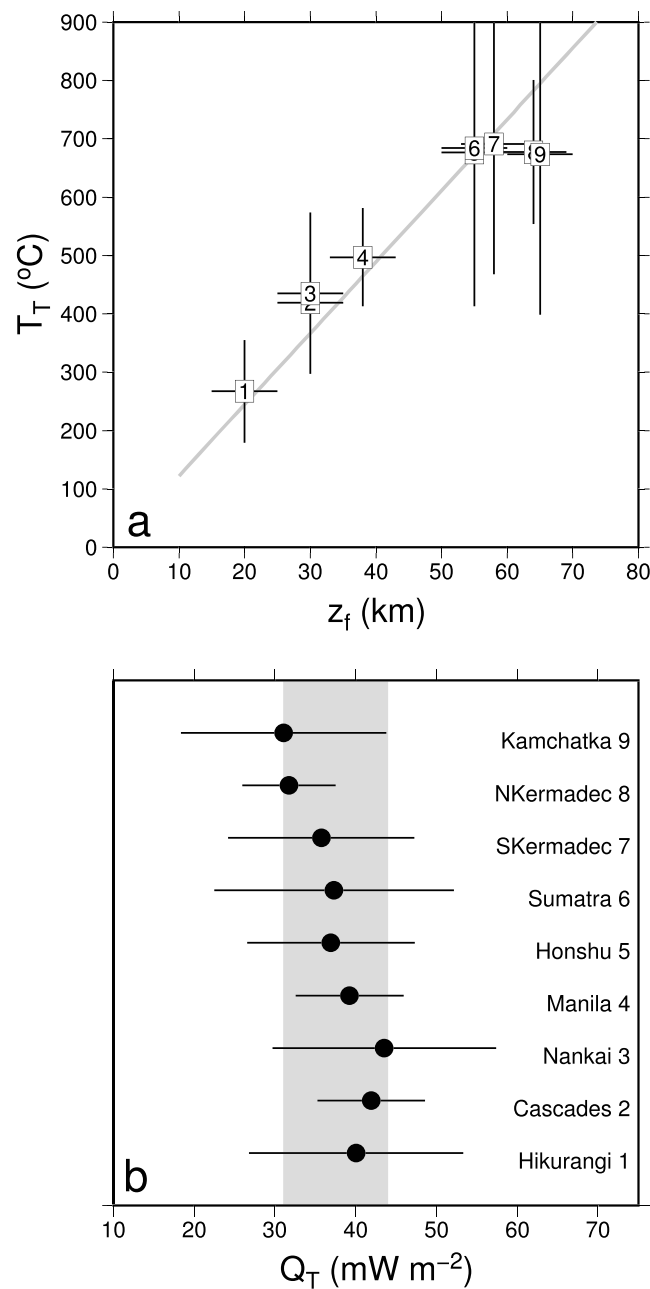


Figure 6. Estimates of temperature, T_T , at maximum depth of thrust-faulting earthquakes and of Q_T (equation (A18)) for the nine heat-flux profiles of Figures 2–4 and B1–B5. (a) Nominal temperatures at maximum depth of thrust faulting for the nine profiles, assuming an average conductivity of $3.0 \text{ W m}^{-1} \text{ K}^{-1}$ for the upper plate. (b) Estimates of Q_T (equation (A18)); bars correspond to mean misfit to surface heat flux for each profile, calculated from equation (16) with unit weights. Grey shading corresponds to $31 < Q_T < 44 \text{ mW m}^{-2}$.

of $3.0 \text{ W m}^{-1} \text{ K}^{-1}$ for the average thermal conductivity of the upper plate, K_1 . Uncertainties in T_T , for this value of K_1 , are calculated from the mean misfit of the heat flux observations for each profile to equation (A14).

With the nominal value of conductivity, the temperature at the maximum depth of thrust-faulting earthquakes varies from about 250°C at 20 km to about 700°C at 60 km (Figure 6a). This range of temperatures contrasts with the roughly constant temperature of about 650°C inferred for the transition between seismic and aseismic strain in the ocean lithosphere (McKenzie et al., 2005) and slabs (Emmerson & McKenzie, 2007; Molnar et al., 1979). Such a contrast is to be expected because of the contrast in lithology between the oceanic upper mantle and the plate interface, which contains a combination of subducted sediment,

oceanic crust, and upper mantle (e.g., Cloos & Shreve, 1988; Fagereng & Sibson, 2010). It is nevertheless the case that the four subduction zones for which the temperatures plotted in Figure 6a lie below $\sim 700^\circ\text{C}$ are also zones with relatively sparse seismic activity, so it is worth examining whether these zones, too, might be characterized by temperatures at the maximum depth of thrust faulting that are close to 700°C . If the estimated temperatures at the assumed maximum depths of thrust faulting are to be increased to 700°C , from the values shown in Figure 6a, then the surface heat flux above the maximum depth would need to be increased by over 60 mW/m^2 for Profile 1 (Figure B1), and by about 30 mW/m^2 for Profiles 2, 3, and 4 (Figures 4, B2, and B3). With the possible exception of the Nankai profile (3, Figure B2), the data do not support this possibility. Alternatively, the estimated maximum depths of thrust faulting for these zones (20–40 km) might underestimate the actual depths. Those estimates are, however, supported by geodetic observations of locking depths and inferred depth extents of historical earthquakes (section 3.1.3 and Appendix B); furthermore, as will be seen in section 3.3, many other subduction segments exhibit maximum depths of thrust-faulting earthquakes in this range. It therefore appears that the variation in T_T shown in Figure 6 is real.

The absolute values of the temperatures in Figure 6a are uncertain to the extent that K_1 is uncertain, which may be up to 25% (Figure A1), but variation in K_1 has the same proportional effect on all temperatures (equation (A17)), so their correlation with z_T is robust. The quantity $K_1 T_T/z_T$ is the surface heat flux above z_T , adjusted for radiogenic heating (equation (A17)), which is determined as part of the analysis. The measurements of Q_T all fall within the range $31 < Q_T < 44\text{ mW/m}^2$ (Figure 6b). In the following section, it is assumed that the transition from seismic to aseismic behavior in subduction zones without heat flux observations takes place at the mean value of Q_T observed here (40 mW/m^2 to one significant figure). When the expressions for stress are written in terms of Q_T (equations (A19) and (A20)), they are independent of the average conductivity of the upper plate, which would otherwise be a significant source of uncertainty (section 2.3 and Appendix A).

3.3. Estimates of Apparent Coefficient of Friction From Maximum Depth of Thrust-Faulting Earthquakes

The maximum depths of thrust-faulting earthquakes are determined for 82 profiles across subduction zones (Appendix C and the supporting information). These measurements are made independently of any assumption about thermal structure and it is reasonable, first, to ask whether they exhibit a systematic behavior that would justify using them to estimate shear stresses.

If μ' and Q_T are fixed, then equation (A20) may be rearranged to give an explicit expression for z_T in terms of the other, known, parameters of the subduction zone:

$$g\bar{\rho}V\mu'z_T - \frac{2Q_TK_2}{K_1}\sqrt{\frac{z_TV_n\sin\delta}{\pi\kappa}} + Q_0 + \frac{AD^2}{2z_T} - Q_T = 0. \quad (17)$$

Figure 7a compares observed values of z_T with those predicted by equation (17) with $\mu' = 0.06$, $Q_T = 40\text{ mW/m}^2$ (the means, to one significant figure, of those quantities determined for the nine heat flux profiles: Figures 5 and 6). The Spearman rank-order correlation coefficient between observed and predicted z_T is 0.53. The significance of this correlation is evaluated by carrying out 10,000 versions of the calculation, in each of which z_T , V , V_n , Q_0 , and δ are perturbed by adding a random Gaussian number times their uncertainties (e.g., Curran, 2015). Uncertainties in V and Q_0 are taken to be 3 mm/year and 10 mW/m^2 , respectively, and uncertainties in δ are propagated from uncertainties of 5 and 10 km for z_T and x_T (section 2.2 and Appendix B). For each version the significance of the correlation is evaluated by Student's t test (routine spear of Press et al., 1992). The distribution of probabilities, $P(R)$, of the correlations, R , having arisen by chance is shown in Figure 7b; 95.5% of the randomly perturbed calculations have a probability of lower than 0.001 of having arisen by chance. This analysis suggests that the distribution of z_T is consistent with a transition from seismic to aseismic slip at a depth corresponding to a narrow range in Q_T and μ' and that it is therefore reasonable to estimate shear stresses for these profiles using the analysis described above and in Appendix A.

For each profile, the maximum depth of thrust-faulting earthquakes is plotted in Figure 8 against the effective shear stress, τ' , corresponding to that depth, calculated from equation (A19) with $Q_T = 40\text{ mW/m}^2$. Radiogenic heat production in the upper plate is unknown for these profiles; the term representing heat production in equation (A19), $AD^2/2z_T$, is allotted a value of zero where the upper plate is oceanic, and for continental upper plates A is set to $2\text{ }\mu\text{W/m}^3$ with D being 15 km. Uncertainty in this term leads only to small uncertainty in τ' because the term SQ_T in equation (A19) is much larger than the heat production term (section 2.3).

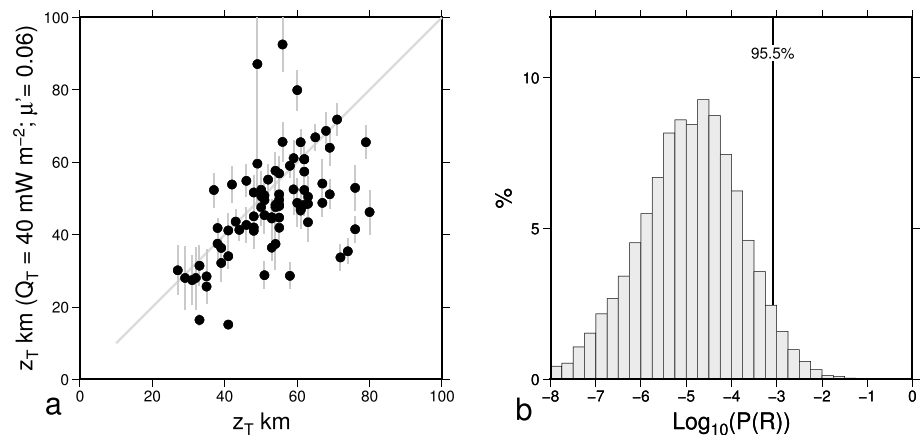


Figure 7. Systematics in variation of measurements of z_T . (a) Dots show z_T measured for 82 profiles across subduction zones (supporting information) plotted against z_T predicted from equation (17) with $\mu' = 0.06$, $Q_T = 40 \text{ mW/m}^2$ (to one significant figure, their mean values in Figures 5 and 6). Bars show the standard deviation of predicted z_T obtained from 10,000 randomly permuted versions of this calculation, as described in the text. (b) Distribution of probabilities that correlations among 10,000 versions of the calculation could have arisen by chance. Vertical line shows the probability below which 95.5% of the permutations fall.

The estimates of τ' increase in proportion to z_T (Figure 8a). The distribution of estimates of apparent coefficient of friction, μ' , corresponding to the estimates of τ' for individual profiles, is shown in Figure 8b and summarized, by subduction zone, in Table 1. The individual profiles are illustrated in the supporting information. The average value of μ' is 0.067, and the estimates are normally distributed with a standard deviation of 0.007, or about 10% of their average value. The principal uncertainty in μ' arises from uncertainty in Q_T (see section 2.3 and equation (15); as discussed above, an effective standard deviation for Q_T is about 4 mW/m^2 , or $\sim 10\%$ of the value of Q_T employed in estimating shear stresses here. This analysis suggests, as does that of the smaller sample of profiles analyzed in section 3.1 (Figure 5), that the range in apparent coefficient of friction across all subduction zones is significantly smaller than has previously been deduced from the modeling of heat flux profiles.

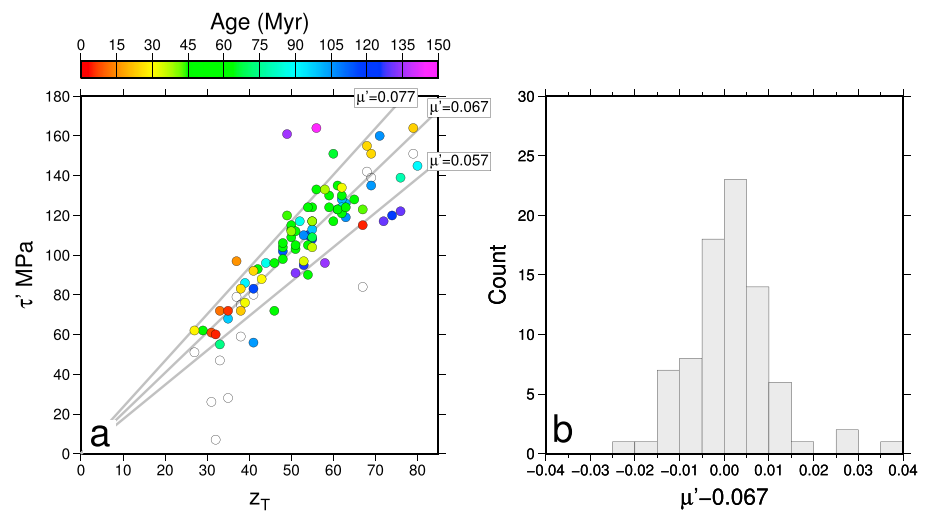


Figure 8. Apparent shear stress and apparent coefficient of friction for 82 profiles across subduction zones. (a) Apparent shear stress, τ' , at maximum depth of thrust-faulting earthquakes, z_T , calculated using equation (A19), with hydrothermal correction to Q_0 (equation (9)). Colors show age of the ocean floor of the lower plate; open symbols show estimates of shear stress, for subduction zones with ocean floor younger than 30 Myr, without the hydrothermal correction to Q_0 . Grey lines correspond to apparent coefficients of friction, as indicated, for an upper-plate density of 3100 kg/m^3 , which is the average for all profiles. (b) Distribution of estimates of apparent coefficient of friction, μ' .

4. Discussion

4.1. Comparison With Other Estimates of Shear Stress

In addition to the estimates summarized in Figure 5b, Tichelaar and Ruff (1993) analyzed sparser heat flux measurements to infer values of μ' for subduction zones in the north-east Pacific, finding $0.03 < \mu' < 0.14$ for Honshu, the Kuriles, and Kamchatka, with lower values corresponding to higher assumed values of AD (see section 2.3). Kao and Chen (1991) estimated μ' to lie in the range ~ 0.05 to ~ 0.12 for the Kyushu-Ryukyu arc.

Temperatures at the transition between seismic and aseismic slip on the subduction interfaces estimated from the profiles of surface heat flux increase from about 250°C at 20 km to about 700°C at 60 km (Figure 6a). The transition from velocity-weakening to velocity-strengthening friction is often estimated, from laboratory experiments, to take place at $\sim 400\text{--}500^{\circ}\text{C}$ (e.g., Blanpied et al., 1991, 1995; den Hartog et al., 2012, 2013). Such experiments are, however, at confining pressures of a few hundred MPa and so do not provide information pertinent to the high-pressure end of Figure 6a. McCaffrey et al. (2008) inferred a transitional temperature of $\sim 100^{\circ}\text{C}$ at a depth of about 15 km based on heat flux measurements at the Hikurangi margin; in the present analysis, the same measurements lead to a transition temperature of $\sim 250^{\circ}\text{C}$ (symbol 1, Figure 6). Kao and Chen (1991) calculated from their estimate of $\mu' \sim 0.1$ that temperatures at the maximum depth of thrust faulting in the Kyushu-Ryukyu arc (40–50 km) are $\sim 800^{\circ}\text{C}$; they used an average conductivity $K_1 = 2 \text{ W m}^{-1} \text{ K}^{-1}$ for the upper plate, that temperature would reduce to $\sim 500^{\circ}\text{C}$ with the conductivity of $3 \text{ W m}^{-1} \text{ K}^{-1}$ used here. Tichelaar and Ruff (1993) found that a value of $\mu' = 0.06$ gave the best fit to all the heat flux measurements available to them, and they used this value to estimate temperatures at the maximum depths of thrust faulting from 11 other subduction zones around the Pacific. With K_1 similar to that used here, they obtained temperatures increasing with the maximum depth of thrust faulting, being in the range 300°C to 350°C for the shallowest depths they considered (~ 25 km) to 550°C to 800°C for depths of 50 to 60 km.

Independent estimates of coefficients of friction on the subduction interface come from analyses of the stresses required to support topographic slopes above the interface (e.g., Barr & Dahlen, 1989; Cattin et al., 1997; Cubas et al., 2013; Dahlen, 1990; Davis et al., 1983; Dielforder, 2017; Lamb, 2006; Suppe, 2007). Several of those estimated coefficients of friction are greater than 0.1 (e.g., Barr & Dahlen, 1989; Cattin et al., 1997; Cubas et al., 2013; Dahlen, 1990; Davis et al., 1983), but other estimates lie in the range 0.02 to 0.1 (e.g., Davis et al., 1983; Dielforder, 2017; Lamb, 2006; Suppe, 2007). Comparison of those estimates with estimates of μ' made here is not straightforward; the former relate to the long-term support of the weight of the rock above the plate interface, whereas the latter relate to stresses during slip on the interface. Nevertheless, those studies support the conclusions of thermal studies that shear stresses on convergent plate boundaries are at the level of a few percent of lithostatic stresses.

4.2. Rheological Implications

Over 90% of the estimates of apparent coefficient of friction in Figure 8b lie within the range 0.067 ± 0.015 . The narrowness of this range suggests that a common process, or set of processes, is involved in slip on the seismogenic portion of the subduction interface. That interface is probably a shear zone of several kilometers' width, containing a melange of sediments and fragments of oceanic crust (e.g., Cloos & Shreve, 1988; Fagereng & Sibson, 2010). Many mechanisms have been suggested to cause low shear stresses on subduction interfaces, including high pore-fluid pressures, intrinsic weakness of minerals or mineral foliation within the shear zone, and a range of processes causing dynamic weakening during slip. A detailed analysis of those suggestions is beyond the scope of this paper; this subsection provides a brief discussion of the implications, for such mechanisms, of the narrow observed range of apparent coefficients of friction. The challenge is to identify a mechanism that could maintain an apparent coefficient of friction within a tight range that is close to, but resolvable different from, zero.

It is commonly accepted that pore pressures in fault zones can approach lithostatic values; furthermore, Rice (1992) showed that in a zone whose permeability decreases strongly with depth, and with a steady supply of pore fluid to its base, the effective normal stress can remain at a small value that is nearly independent of depth. Rice confined his analysis to depths appropriate to continental strike-slip faulting (~ 15 km) but subduction interfaces share key elements of the analysis, being low-permeability zones in which fluid is being released by compaction and dehydration reactions. It therefore seems reasonable that, on an individual subduction interface, high pore-fluid pressure might lead to a low effective coefficient of friction that varies little with depth. Two further steps are required, however, if this mechanism is to explain the near constancy of μ' among different subduction segments. First, the analysis addresses the static effective normal stress;

it would not hold if pore fluid pressure were to vary during slip (see below). Second, the magnitude of the effective normal stress depends on three quantities: the permeability of the fault zone at zero effective stress, a material constant that encapsulates the sensitivity of permeability to confining stress, and the fluid flux into the bottom of the fault zone (Rice, 1992, top of p. 493). Those quantities are, in current understanding, likely to vary considerably among subduction zones (e.g., Saffer, 2014; Saffer & Tobin, 2011). If it were to be assumed that high pore fluid pressure accounts for the small range of μ' ($\pm 20\%$, Figure 8b) over subduction interfaces whose bases range in depth from 20 to 60 km, and in temperature from 250°C to 700°C (Figures 6a and 8), then strong constraints could be imposed on the variability of physical properties on those interfaces.

Laboratory experiments suggest that intrinsically weak minerals and rock fabrics may have coefficients of friction as low as ~ 0.1 (e.g., Carpenter et al., 2012; Ikari et al., 2009; Lockner et al., 2011). If such materials were to be in a regime of hydrostatic pore pressure, then the effective coefficient of friction would be similar to the values of μ' (~ 0.07) determined here. Rocks believed to represent such environments are highly heterogeneous in lithology and exhibit deformation that ranges from distributed ductile shear to displacement across discrete slip surfaces (e.g., Fagereng & Sibson, 2010). If deformation of this material is characterized by intrinsically low coefficients of friction, those must vary by only about $\pm 20\%$ (Figure 8b) over temperatures that range from $\sim 200^\circ\text{C}$ to $\sim 700^\circ\text{C}$ and pressures between about 1 and 2 GPa (Figure 8).

High pore fluid pressure, or low intrinsic coefficients of friction, or a combination of both, could explain static stresses on the subduction interface that are close to the measured apparent stresses shown in Figure 8. Neither condition is essential, however, because once slip starts across a fault zone, a number of processes can considerably reduce shear stress below static levels; these include flash heating, thermal pressurization of pore fluid, and thermal decomposition or melting (e.g., Di Toro et al., 2006; Goldsby & Tullis, 2011; Lachenbruch, 1980; Nielsen et al., 2016; Platt et al., 2015; Rempel & Rice, 2006; Rice, 2006, 2017; Sibson, 1973, 1975). Although it is evident that such processes can limit shear stress during slip, it remains to be seen whether any of them could lead to apparent coefficients of friction that are effectively constant across a wide range of subduction zones.

I address this question using Rice, 's (2006) analysis of thermal pressurization of pore fluid during slip. There are two reasons for concentrating on this mechanism. First, subduction interfaces contain fluids throughout the depth range of interest, so pore fluid pressurization is likely during all earthquakes within them. (e.g., Lachenbruch, 1980; Rice, 2006; Sibson, 1973). Second, the mechanism can be analyzed in a simple fashion because Rice (2006) provided a description of the weakening that depends on a single parameter. The average shear stress during slip of magnitude u on a fault whose shear stress is controlled by thermal pressurization of pore fluid is

$$\bar{\tau}(u) = \frac{1}{u} \int_0^u \tau(u') du' = \sigma_n \mu_0 (1 - \lambda) \frac{L^*}{u} \left[\exp\left(\frac{u}{L^*}\right) \operatorname{erfc}\left(\sqrt{\frac{u}{L^*}}\right) + 2\sqrt{\frac{u}{\pi L^*}} - 1 \right], \quad (18)$$

(Rice, 2006, equation (30)), where σ_n is the normal stress, μ_0 and λ are the coefficient of friction and the ratio of pore fluid pressure to normal stress at the start of slip, and L^* is a characteristic slip over which weakening takes place

$$L^* = \left(\frac{2\rho c}{\mu_0 \Lambda} \right)^2 \frac{(\sqrt{\alpha_h} + \sqrt{\kappa})^2}{V_*}. \quad (19)$$

Here ρc is volumetric heat capacity, Λ is the coefficient of thermal pressurization, which relates increases in pore-fluid pressure to increases in temperature, α_h is the hydraulic diffusivity, and V_* is the rate of slip. (The notation differs from that of Rice, 2006, to avoid multiple assignments to the symbols δ and V and to retain κ and μ as used here.) Once $u > L^*$, significant weakening takes place during slip: $\bar{\tau}(u)$ is half the static value or lower (Rice, 2006, Figure 3).

$\bar{\tau}(u)$ in equation (18) is related to the apparent stress, τ' , in that when multiplied by the displacement, u , it gives the heat supplied per unit area. However, $\bar{\tau}$ relates to a single earthquake, whereas τ' depends on the heat supplied by all earthquakes, so the apparent coefficient of friction must be obtained by integrating equation (18) across the distribution of earthquakes on the interface. Expressions are derived for τ' and μ' in Appendix D for a fault zone in which the frequency of earthquakes is inversely proportional to their moments raised

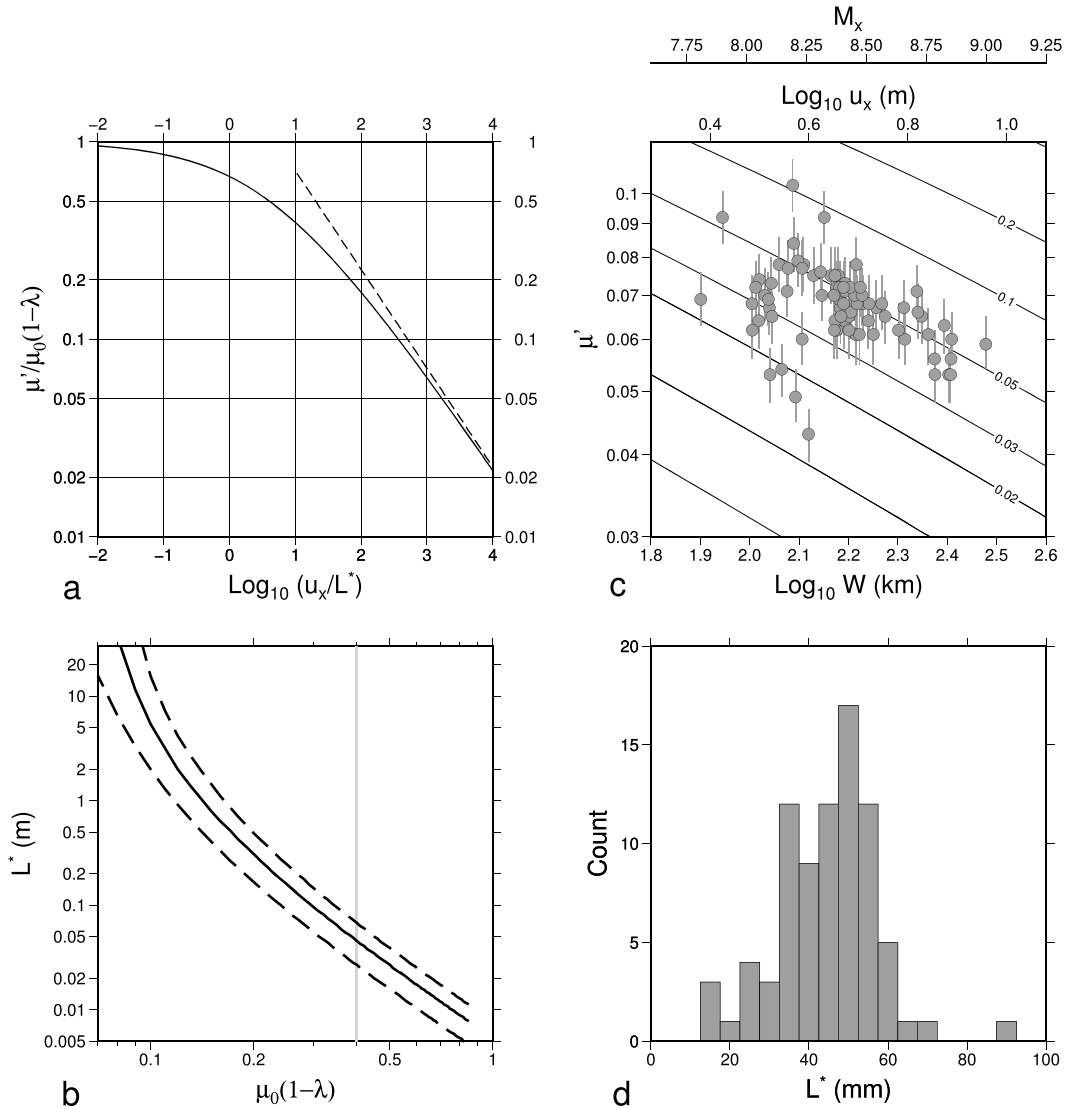


Figure 9. Theoretical and observed relations between apparent coefficient of friction, μ' , and maximum slip, u_x , during earthquakes on a subduction interface. (a) Ratio of apparent coefficient of friction during slip, μ' , to $\mu_0(1 - \lambda)$, from the expression of Rice (2006, equation (30)) applied to a Gutenberg-Richter distribution of earthquakes with $\beta = 2/3$ (Appendix D, and equation (20)). Dashed line corresponds to equation (22). (b) Black line shows value of L^* , for a given $\mu_0(1 - \lambda)$, that yields (via equation (20)) the best fit to observed values of μ' (Figure 8), with $u_x = 3 \times 10^{-5} W$ (see equation (23)). Dashed lines delimit the range of L^* for which the root-mean-square misfit is smaller than twice the minimum misfit (see text). Grey line indicates the condition $\mu_0(1 - \lambda) = 0.4$, which is illustrated in (c). (c) Contours show the dependence of μ' on u_x (equation (20)) for the values of L^* (in meters) given by the labels, with $\mu_0(1 - \lambda) = 0.4$. Circles show downdip width of the zone of thrust-faulting earthquakes, W , for the profiles of Figure 7, plotted against μ' for those profiles with u_x given by equation (23). Bars correspond to 10% uncertainty in μ' , arising from a comparable uncertainty in Q_T (equation (15)), Section 2.3). (d) Distribution of L^* for the W - μ' observations plotted in (c).

to a power, β (equations (D9) and (D10)). It is commonly the case that $\beta \sim 2/3$, in which case the expression derived in Appendix D for the apparent coefficient of friction (equation (D10)) reduces to

$$\mu' = \mu_0(1 - \lambda) \frac{L^*}{u_x} \int_0^{u_x} \frac{1}{u} \left[\exp\left(\frac{u}{L^*}\right) \operatorname{erfc}\left(\sqrt{\frac{u}{L^*}}\right) + 2\sqrt{\frac{u}{\pi L^*}} - 1 \right] du \quad (20)$$

where u_x is the slip in the greatest earthquakes taking place on the interface. In the limits of low slip and high slip, equation (20) simplifies to

$$u_x/L^* \rightarrow 0 \quad \mu' \rightarrow \mu_0(1 - \lambda)' \quad (21)$$

$$u_x/L^* \gg 1 \quad \mu' \sim 4\mu_0(1-\lambda) \sqrt{\frac{L^*}{\pi u_x}}. \quad (22)$$

The dependence of μ'/μ_0 on u_x/L^* is shown in Figure 9a.

The magnitude of the slip-weakening distance, L^* , is poorly constrained because it depends on a combination of physical properties of the fault zone, two of which are particularly uncertain—the permeability, which enters into the hydraulic diffusivity α_h , and the coefficient of thermal pressurization, Λ . The coefficients of friction and pore fluid pressures on subduction faults are also poorly known. It can be seen from equation (20) that observations of μ' place constraints on the ratio of $\mu_0(1-\lambda)$ to L^*/u_x , but not on either separately. If, however, u_x can be estimated for each profile, equation (20) may be used to identify a narrow range in $L^* - \mu_0(1-\lambda)$ parameter space that is consistent with the observed range of apparent coefficients of friction, μ' . The maximum slip, u_x , cannot be estimated from the earthquake records for each segment, which are too short to ensure that the maximum magnitude of earthquakes has been observed (e.g., McCaffrey, 2008; Rong et al., 2014; Stein & Okal, 2007). To circumvent this difficulty, I assume that the maximum moment, M_x , of earthquakes in a given subduction zone is proportional to the downdip width, W , of the interface over which thrust-faulting earthquakes occur. This assumption is motivated by Hayes et al.'s (2012, Figure 11) demonstration of a correlation between W and the maximum recorded magnitudes of earthquakes upon them. Following Hayes et al. (2012), W is taken to be the distance along the slab from depth of 10 km to z_T . The relation between u_x and W is taken from the observations of Ye et al. (2016), who show that for large and great earthquakes in subduction zones

$$M \sim 2 \times 10^6 \Delta \Sigma^{3/2} \quad (23)$$

with moment, M , in Newton meters and area of fault plane, $\Delta \Sigma$, in meter squared (Ye et al., 2016, Figure A1b). Assuming that $\Delta \Sigma \sim W^2$ then, for a shear modulus of 50 GPa, $u_x \sim 3 \times 10^{-5} W$ (see also Wells & Coppersmith, 1994).

The solid line in Figure 9b shows the values of L^* that provide the best fit to the observed values of μ' , for the 82 profiles summarized in Figure 8, as $\mu_0(1-\lambda)$ varies from 0.07 to 0.85. The upper limit on $\mu_0(1-\lambda)$ corresponds to Byerlee's rule with zero pore pressure and low confining stress (Byerlee, 1978), while the lower limit reflects the fact that fits are meaningless once $\mu_0(1-\lambda)$ becomes comparable with the observed range of μ' because, as $\mu_0(1-\lambda) \rightarrow \mu'$, $L^*/u_x \rightarrow \infty$ (equation (21)). The best fitting value of L^* for $\mu_0(1-\lambda) = 0.4$, the case illustrated in Figure 9c, is 46 mm, with an RMS misfit to μ' of 0.007 and a range of $26 \text{ mm} < L^* < 68 \text{ mm}$ giving misfit less than twice this value.

Figure 9c plots the observed relationship between μ' and W (hence u_x , equation (23)) against the relationship predicted by equation (20) with $\mu_0(1-\lambda) = 0.4$. That value is chosen to illustrate the behavior of a fault zone conforming to Byerlee's rule with high confining stress and hydrostatic pore-fluid pressure ($\mu = 0.6$, $\lambda \sim 0.3$). The dependence of μ' on W shows a remarkable conformity with what would be expected were frictional stress during slip on the subduction interface to be controlled by thermal pressurization (equation (20)). The quality of fit is maintained across the relevant range of $\mu_0(1-\lambda)$; all that changes is that higher values of $\mu_0(1-\lambda)$ require lower values of L^* in order to fit the observed values of μ' , and vice versa, as can be understood from equation (20) and Figure 9a. The RMS misfits between calculated and observed values of μ' remain less than 0.007 (10% of the mean value of μ') for the whole range $0.07 < \mu_0(1-\lambda) < 0.85$.

With $\mu_0(1-\lambda) = 0.4$, 80% of the measured values of μ' lie within the range $30 \text{ mm} \leq L^* \leq 60 \text{ mm}$ (Figures 9c and 9d), with that range dropping to $10 \text{ mm} \leq L^* \leq 25 \text{ mm}$ for $\mu_0(1-\lambda) = 0.6$ which, corresponding to Byerlee's rule with high confining stress and zero pore-fluid pressure, represents a plausible upper limit for subduction settings. Recall that L^* is the slip-weakening distance; as L^* decreases, the minimum magnitude at which earthquakes become affected by thermal pressurization decreases (equation (18)). For high static strengths of the fault ($\mu_0(1-\lambda) \gtrsim 0.2$), when L^* is a few centimeters to decimeters, significant weakening occurs for earthquakes as small as $M_w \sim 2-3$. If the static strength of the fault is low ($\mu_0(1-\lambda) \lesssim 0.1$) then L^* is required to be $\gtrsim 3-10 \text{ m}$ meaning that, for μ' to remain comparable with $\mu_0(1-\lambda)$, even great earthquakes must remain unaffected by thermal pressurization. At the lower end of the range (a few centimeters), the values of L^* estimated here are about 10 times greater than those calculated by Brantut and Platt (2017) for subduction zones, assuming that the faults are dominated by the properties of olivine. Estimates of L^* from fracture energies in earthquakes give a range from a few millimeters to a few centimeters (Rice, 2006).

Although most of those estimates are from small earthquakes in continental crust, the few large earthquakes in the data set of Rice (2006) are fit by the same range of L^* .

The consistency between the observed dependence of μ' on W and that predicted by a model of thermal pressurization (Figure 9c) is compelling but should not be taken as demonstration that this process dominates earthquake slip on subduction zones. Rice's (2006) model contains several simplifying assumptions and the calculation of key parameters in that model from laboratory measurements of physical properties carries many uncertainties (e.g., Brantut & Platt, 2017). Furthermore, other mechanisms such as elastodynamic weakening, flash heating, or slip on phyllosilicate networks in a fault zone may lead to very low apparent coefficients of friction (e.g., Andrews & Ben-Zion Y., 1997; Ben-Zion & Ampuero, 2009; Beeler et al., 2008; Collettini et al., 2009; Fagereng & den Hartog, 2016; Goldsby & Tullis, 2011; Lomnitz-Adler, 1991).

4.3. Implications for Maximum Magnitudes of Earthquakes

The maximum recorded magnitudes, M_x , of earthquakes on individual sections of convergent plate boundaries range from M_w 7 to M_w 9.6 (e.g., Stein & Okal, 2007). It is of central importance to the assessment of seismic hazard and risk to understand whether that range represents the actual long-term distribution of earthquake magnitudes, and in particular whether subduction zones with historically low maximum magnitudes may in the future be exposed to much larger earthquakes (e.g., McCaffrey, 2008; Rong et al., 2014; Stein & Okal, 2007). There have been numerous attempts to correlate the parameters of subduction zones with past maximum magnitudes of earthquakes (e.g., Gao & Wang, 2014; Hardebeck & Loveless, 2017; Hayes et al., 2012; Heuret et al., 2011, 2012; Jarrard, 1986; Kelleher et al., 1974; McCaffrey, 2008; Pacheco et al., 1993; Ruff, 1989, 1980; Scholz & Campos, 1995, 2012; Schellart & Rawlinson, 2013; Stein & Okal, 2007), but there is no agreement as to which, if any, of those parameters provides a reliable proxy for future maximum magnitudes.

Two recent studies directly relate M_x to the apparent coefficient of friction, μ' , as determined here. Those studies (Gao & Wang, 2014; Hardebeck & Loveless, 2017) compared μ' with the fraction of the relative motion across the plate interface that is accommodated by slip in earthquakes. That fraction is often termed *coupling*, but the same label is also used to describe several other aspects of subduction zones (see, e.g., Wang & Dixon, 2004). To avoid confusion, the fraction is referred to here by the symbol χ (e.g., Scholz & Campos, 1995, 2012). Subduction zones in which most of the relative motion is accommodated aseismically would have low χ ; zones in which all the relative motion is accommodated by earthquakes would have $\chi = 1$. Gao and Wang (2014) proposed that the greatest earthquakes take place in subduction zones that have high values of χ and low values of μ' ; in contrast, Hardebeck and Loveless (2017) argued that the greatest earthquakes are associated with subduction zones with high χ and high μ' .

There are substantial impediments to using μ' or χ as a proxy for maximum earthquake size in a given subduction zone. The observed range of μ' derived from heat flux measurements (Figure 5) is approximately 40% of their mean value, and for μ' derived from z_T (Figure 7) the range is 20% of their mean value. In each case, the range is approximately the size of the uncertainties, so variation in μ' is unresolved. Seismic estimates of χ cannot be used as a proxy: the dominant uncertainty in such an estimate is whether the quantity of interest—the greatest earthquake magnitude in a given zone—is represented in the record (e.g., Brune, 1968; McCaffrey, 2008; Rong et al., 2014; Stein & Okal, 2007). Geodetic estimates of χ may eventually prove reliable, but at present they too, are problematic because they can be time-dependent (e.g., Loveless & Meade, 2016; Marsan et al., 2017; Mavrommatis et al., 2015; Yokota & Koketsu, 2015), and, until sea-floor GPS becomes more widespread, it will remain difficult to resolve the degree to which offshore segments of plate boundaries are locked or slipping. Schellart and Rawlinson (2013) investigated the correlations between a further 24 subduction zone parameters and maximum recorded magnitudes of earthquakes, finding that, globally, none of the correlations is significant.

Hayes et al. (2012), however, showed that the downdip width of the subduction interface, W , correlates with maximum magnitude of earthquakes (see also Kelleher et al., 1974; Suarez & Sánchez, 1996). This correlation is reasonable because great earthquakes tend to rupture through most of the seismogenic depth range of the subduction interface. Figure 10 shows the relationship between maximum magnitudes of earthquakes from Stein and Okal (2007), updated by Hayes et al. (2012), and the downdip width of the seismogenic part of the interface, W , observed in the present study (Table 1). The grey lines in this figure show the relationship that would be expected if the greatest earthquake on a given subduction segment had an area equal to W^2 and moment given by equation (23) (Ye et al., 2016). Most of the subduction zones have M_x that is at least as great as would be expected from their observed W ; indeed, M_x generally lies well above this line,

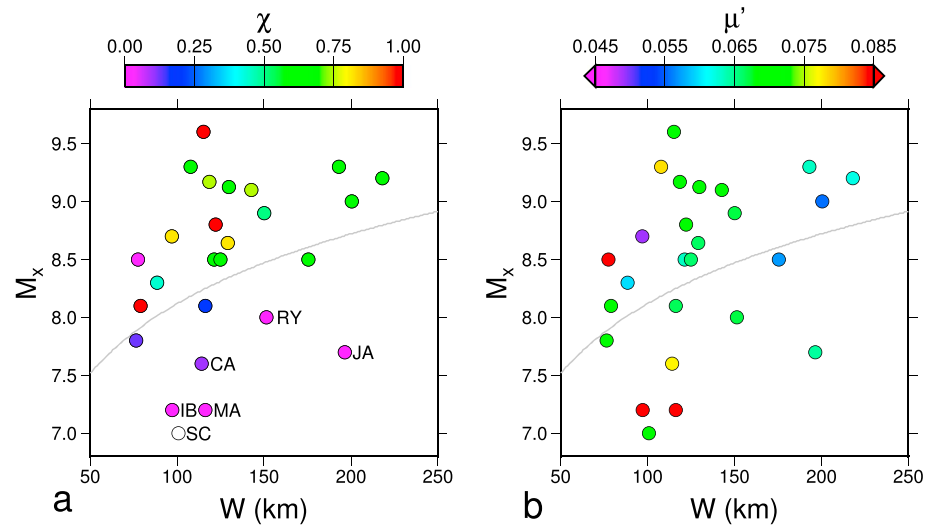


Figure 10. Relation between maximum recorded magnitude, M_x , of earthquakes in subduction zones and the downdip extent of the seismogenic interface, W , after Hayes et al. (2012). M_x from Stein and Okal (2007), updated by Hayes et al. (2012); W from the present study, averaged for the subduction segments of Stein and Okal (2007; Table 1). (a) Colors (scale at top) indicate the proportion, χ , of relative motion in each zone that is accommodated seismically (estimated by Scholz & Campos, 1995, 2012). Grey line corresponds to the relation between moment and W given by equation (23). Subduction zones for which the maximum recorded magnitude lies more than 0.5 of a unit below the grey line are labeled as follows: RY = Ryukyu; CA = Central America; JA = Java; IB = Izu-Bonin; MA = Marianas; SC = Scotia. (b) As in (a) except that colors relate to the average value of μ' determined for the subduction zone (Table 1).

which is reasonable, because most great earthquakes extend along strike by considerably more than the down-dip width of the seismogenic interface.

For six of the 28 segments, however, the recorded maximum magnitudes are half a magnitude unit or more below what is expected for their seismogenic widths. All those segments are thought to have $\chi \lesssim 0.1$ (Scholz & Campos, 1995, 2012, and Figure 10a) and it is important to determine whether χ genuinely is low in these subduction zones, or whether they are capable of hosting earthquakes much greater than have so far been recorded there. It should be recalled that both the 2004 Sumatra and 2011 Tohoku earthquakes exceeded the expected maximum magnitudes for those subduction zones by at least half a unit (e.g., Rong et al., 2014; Stein & Okal, 2007, 2011).

If thermal pressurization in earthquakes controls the apparent coefficient of friction on the plate interface, as suggested in section 4.2, then the measurements of μ' made here cast light on the maximum sizes of earthquakes. The values of μ' for the six zones in question (Table 1) differ from the average value for all zones by 0% (Java, Ryukyu), 5% (Scotia), ~15% (Central America), and 40–50% (Izu-Bonin, Mariana), while their apparent values of χ are all close to zero (apart from the Scotia arc, where it is unknown). If those values of χ were to represent the long-term rate of moment release in earthquakes, then the coefficient of friction associated with aseismic slip (which would be taking up 90–100% of the relative motion in these subduction zones) must be similar to the apparent coefficient of friction for seismic slip in the other zones, where the relative motion is accommodated primarily by earthquakes. Alternatively, the similarity in μ' between the six zones with low χ and those with high χ may suggest that they share the same mechanism of heat generation, therefore that these zones, too, are prone to great earthquakes.

This argument does not go so far as to suggest that all subduction zones are capable of hosting an earthquake of $M_w \gtrsim 9$ (e.g., McCaffrey, 2008; Rong et al., 2014). It does, however, suggest that a prudent approach to the hazard would be to assume that any given subduction zone is capable of hosting an earthquake at least as large as would be predicted from the downdip length, W , of its seismogenic interface (Hayes et al., 2012; Kelleher et al., 1974; Suarez & Sánchez, 1996). The maximum magnitude could be considerably larger than this because great earthquakes typically rupture several adjacent patches of the interface. Whether or not adjacent patches do rupture in a single event may depend on tectonic contributions to the normal stress

on the interface (e.g., Schellart & Rawlinson, 2013; Scholz & Campos, 2012, 1995), on curvature or irregularity of the plate boundary (e.g., Bletery et al., 2016; Schellart & Rawlinson, 2013) or on other factors peculiar to individual boundary segments.

5. Conclusions

Apparent coefficients of friction determined from nine heat flux profiles above convergent plate boundaries lie, with the exception of that for the North Cascades which is unconstrained, in the range $0.05 \lesssim \mu' \lesssim 0.07$ (section 3.1 and Figure 5). Although previous interpretations of these profiles delivered estimates of μ' between zero and > 0.15 , uncertainties in those estimates usually were not quantified. When account is taken of the uncertainties associated with the heat flux measurements and with estimates of radiogenic heating in the upper plate, differences between previous estimates and those obtained here are not significant (Figure 5). Furthermore, the uncertainties in individual determinations of μ' exceeds their range, so differences among apparent coefficients of friction derived from the heat flux measurements are unresolved.

A quantity Q_T , which is the surface heat flux above the maximum depth of thrust faulting earthquakes, z_T , adjusted for radiogenic heating in the upper plate (Section A1, equation (A18)), lies within the range 31–44 mW/m² for all nine profiles (Figure 6b and section 3.2). This relation implies that the transition from seismic to aseismic slip takes place at a temperature, T_T , that depends on depth; with a nominal value of 3 Wm^{−1} K^{−1} for the average conductivity of the upper plate, $T_T \sim z_T \times 12^\circ\text{C}/\text{km}$ (Figure 6a and section 3.2).

The assumption of a constant value of Q_T , which is shown to be reasonable (Figure 7), allows estimation of apparent stress on a further 82 profiles across subduction zones. Shear stresses at the maximum depth of thrust-faulting earthquakes vary from ~ 40 to ~ 160 MPa, and yield estimates of the apparent coefficient of friction on the plate interface of $\mu' = 0.07 \pm 0.01$ (section 3.3 and Figure 8). The observed narrow range of apparent coefficients of friction can be explained if heat is generated on the subduction interfaces primarily during earthquakes in which the shear stress is modulated by thermal pressurization of pore fluids. Rice's (2006) analysis of this process, when applied to a Gutenberg-Richter distribution of earthquakes, predicts an inverse dependence of μ' on u_x , the maximum slip in earthquakes on the subduction interface and hence on W , its downdip extent (section 4.2 and Appendix D). The observed relationship between μ' and W agrees with that prediction (Figure 9). It therefore appears that, rather than the coefficient of friction on subduction interfaces controlling maximum magnitudes of earthquakes (e.g., Gao & Wang, 2014; Hardebeck & Loveless, 2017), the maximum slip in earthquakes controls the apparent coefficient of friction (equation (20) and Figure 9c).

Apparent coefficients of friction on subduction interfaces where the fraction, χ , of the relative motion that is accommodated seismically has been historically low are indistinguishable from those in which relative motion has been accommodated primarily in earthquakes. Until reliable, long-term, estimates of χ become available, a prudent approach to the seismic hazards is to assume that the mechanisms of slip are the same, therefore that any subduction zone is capable of generating an earthquake of $M_w \gtrsim 8.5$ (Figure 10) (e.g., Hayes et al., 2012; Kelleher et al., 1974; Marzocchi et al., 2016; McCaffrey, 2008; Rong et al., 2014; Suarez & Sánchez, 1996).

Appendix A: Mathematical Development

A1. Approximate Analytical Expressions for Temperature and Surface Heat Flux

Consider a subduction interface that separates an upper plate of average conductivity K_1 from a lower plate whose conductivity near its upper surface is K_2 (Figure 1). Temperatures on the interface may be obtained, to a good approximation, by treating the lower plate as a semi-infinite medium, $0 < y < \infty$ whose surface ($y = 0$) is held at a temperature

$$T(0, t) \propto t^{m/2}, \quad (\text{A1})$$

where m is a positive integer and t is time since the top of the lower plate passed beneath the upper plate (Molnar & England, 1990). For initial temperature $T = 0$ throughout the lower plate, the heat flux out of its surface is

$$-K_2 \frac{\partial T}{\partial y} = K_2 \frac{\Gamma(m/2 + 1)}{\Gamma(m/2 + 1/2)} \frac{T(0, t)}{\sqrt{\kappa t}}, \quad (\text{A2})$$

(Carslaw & Jaeger, 1959, p. 63), where κ is thermal diffusivity and Γ is the gamma function. Molnar and England (1990) show that if the principal source of heat is the heat flux from the lower plate, Q_0 , then temperatures on the interface increase approximately in proportion to \sqrt{t} ; hence, $m = 1$. If, however, heating on the interface dominates and—as assumed here—is proportional to depth, then temperatures on the interface increase approximately in proportion to $t^{3/2}$; hence, $m = 3$. For the cases of interest in this paper, the two sources are of the same order of magnitude, and temperatures increase on the interface approximately in proportion to t , hence m is taken to be 2, and $\Gamma(m/2 + 1) / \Gamma(m/2 + 1/2) = 2/\sqrt{\pi}$ (Abramowitz & Stegun, 1970).

For a point at depth z_f on the subduction interface, equation (A2) may be written as

$$K_2 \frac{\partial T}{\partial y} = - \frac{2K_2 T_f}{\sqrt{\pi \kappa z_f / (V_n \sin \delta)}}, \quad (\text{A3})$$

where T_f is the temperature on the interface at the depth z_f , δ is the average dip above z_f , and V_n is the component of relative plate motion in the direction parallel to the dip of the interface. Although most plate interfaces vary in dip, comparison of equations (A2) and (A3) shows that the important variable is the time, t , taken for the lower plate to reach depth z_f ; therefore, that formulation of the problem in terms of the average dip of the interface is justified. After a time interval $t_1 \sim z_f^2 / (\pi^2 \kappa)$ following the initiation of subduction, the temperatures on any vertical profile passing through both plates are independent of time (Molnar & England, 1990, Figures 2–4). Expressions given here apply to that steady state.

First, consider the case in which radiometric heating and dissipative heating may be neglected. Let Q_0 be the heat flux through the surface of the lower plate immediately before it enters the trench. When the top of the lower plate has reached a depth z_f , this flux is diminished as described by equation (A3) and the heat flux into the base of the upper plate is

$$Q_2 = Q_0 - \frac{2K_2 T_f}{\sqrt{\pi \kappa z_f / (V_n \sin \delta)}}. \quad (\text{A4})$$

In the absence of heat production, Q_2 is equal to the heat flux throughout the upper plate

$$Q_0 - \frac{2K_2 T_f}{\sqrt{\pi \kappa z_f / (V_n \sin \delta)}} = \frac{K_1 T_f}{z_f}, \quad (\text{A5})$$

$$T_f = \frac{Q_0 z_f}{K_1 S},$$

where

$$S = 1 + \frac{2K_2}{K_1} \sqrt{\frac{z_f V_n \sin \delta}{\pi \kappa}}. \quad (\text{A6})$$

If, additionally, dissipative heating occurs at a rate $\tau'V$ per unit area on the subduction interface, then

$$Q_1 = Q_2 + \tau'V, \quad (\text{A7})$$

$$T_f = \frac{(Q_0 + \tau'V) z_f}{K_1 S}. \quad (\text{A8})$$

When a constant rate of heat production per unit volume, A , to a depth D within the upper plate is included, the temperature of the interface becomes

$$T_f = \frac{(Q_0 + \tau'V) z_f + AD^2/2}{K_1 S}, \quad (\text{A9})$$

where D is the lesser of z_f and D .

These expressions are similar to those of Tichelaar and Ruff (1993) and Molnar and England (1990, 1995), although here K_1 applies to the appropriately averaged thermal conductivity of the upper plate, and K_2 applies only to the upper part of the lower plate where $T \sim T_f$.

The expression for temperatures below the fault is given for completeness, although it is not needed in the analysis of this paper:

$$T(y, t) = 4T_f i^2 \operatorname{erfc} \left(\frac{y}{2\sqrt{\kappa t}} \right) \quad (\text{A10})$$

(Carslaw & Jaeger, 1959, p. 63), where $i^2 \operatorname{erfc}$ is the second integral of the complementary error function (Abramowitz & Stegun, 1970).

In each of equations (A5), (A8), and (A9) temperatures along the plate interface are directly related to the solution to the one-dimensional steady state thermal conduction equation

$$\frac{d^2 T}{dz^2} = -\frac{\mathcal{A}(z)}{K_1} \quad (\text{A11})$$

where $\mathcal{A}(z)$ is the rate of heat production, including both radiogenic heating in the upper plate and dissipative heating on the plate interface:

1. If the only source of heat is a basal heat flux Q_0 , then

$$T(z) = \frac{Q_0 z}{K_1}.$$

2. If the only source of heat is heating at a rate A to a depth, D , then

$$T(z) = \frac{A}{K_1} \left(Dz - \frac{z^2}{2} \right), \quad z \leq D \quad T(z) = \frac{AD^2}{2K_1}, \quad z \geq D.$$

3. If the only source of heat is heat liberated at a rate τV at depth z_f , then

$$T(z) = \frac{\tau V z_f}{K_1}, \quad z \leq z_f \quad T(z) = \frac{\tau V z_f}{K_1}, \quad z \geq z_f.$$

It can be seen, by adding the relevant combinations of the expressions above with $z = z_f$, that temperatures on the interface are given by the 1-D steady state solutions divided by a factor, S (Molnar & England, 1990).

The surface heat flux, Q_s , is the sum of the heat flux into the base of the upper plate and the radiogenic heat production per unit area within it:

$$Q_s = Q_1 + AD \quad (\text{A12})$$

$$Q_s = \frac{Q_0 + \tau' V}{S} + AD \left[1 - \frac{D}{2z_f} \left(1 - \frac{1}{S} \right) \right] \quad (\text{A13})$$

$$= \frac{Q_0 + \mu' g \bar{\rho} z_f V}{S} + AD \left[1 - \frac{D}{2z_f} \left(1 - \frac{1}{S} \right) \right]. \quad (\text{A14})$$

In obtaining equations (A13) and (A14), the expression for T_f (equation (A9)) has been substituted into equation (A4) to give Q_2 hence, through equation (A7), Q_1 .

The relationships between surface heat flux, shear stress, τ' , on the interface, and μ' are, from equations (A13) and (A14),

$$\tau' V = S \left(Q_s - AD \left[1 - \frac{D}{2z_f} \left(1 - \frac{1}{S} \right) \right] \right) - Q_0, \quad (\text{A15})$$

$$\mu' = \left[S \left(Q_s - AD \left[1 - \frac{D}{2z_f} \left(1 - \frac{1}{S} \right) \right] \right) - Q_0 \right] / g \bar{\rho} z_f V. \quad (\text{A16})$$

Temperatures on the plate interface are related to the surface heat flux by

$$T_f = \frac{z_f}{K_1} \left[Q_s - AD \left(1 - \frac{D}{2z_f} \right) \right]. \quad (\text{A17})$$

Analysis of heat-flux profiles across nine subduction zones in section 3.2 shows that temperatures, T_T , at the maximum depths of thrust-faulting earthquakes in those zones, z_T , are proportional to z_T :

$$\frac{K_1 T_T}{z_T} = Q_T \sim \text{constant}. \quad (\text{A18})$$

The value of Q_T obtained in section 3.2 is used in section 3.3 to estimate apparent shear stresses at z_T . Combining equation (A9) with equation (A18)

$$\tau' = \frac{S Q_T - Q_0 - A D^2 / (2 z_T)}{V}, \quad (\text{A19})$$

$$\mu' = \frac{S Q_T - Q_0 - A D^2 / (2 z_T)}{g \bar{\rho} z_T V}. \quad (\text{A20})$$

For many purposes in the present analysis, $z_T > D$; the forms of equations (A14), (A17), and (A19) relevant to this condition are given in equations (4), (5), and (7) of section 2.

A2. Influences of Variable Thermal Conductivity

The analytical expressions of Molnar and England (1990) assume constant thermal conductivity; this assumption needs to be relaxed because the thermal conductivity of rocks depends strongly on their temperature (e.g., Furlong & Chapman, 2013; Whittington et al., 2009; Xu et al., 2004, and Figure A1). Variation of thermal conductivity with temperature influences the analysis in important ways at two points. First, all estimates of temperature on the plate interface depend upon the average thermal conductivity of the upper plate (e.g., equation (A9)). Second, the factor S , which is central to the analysis, depends upon the ratio of the conductivity at the top of the lower plate to the average conductivity of the upper plate (equation (A6)).

Furlong and Chapman (2013) gave expressions for heat capacity and thermal diffusivity of crustal rocks which yield an almost twofold reduction in thermal conductivity between 300 and 800 K (black line in Figure A1a). Xu et al. (2004) proposed a relation for the temperature-dependence of thermal conductivity of olivine of the form

$$K(T) \sim K_0 \left(\frac{T_0}{T} \right)^p, \quad (\text{A21})$$

where T is temperature in kelvins. Xu et al. (2004) use $p = 1/2$, $T_0 = 298$ K, and $K_0 = 4.1$ W·m·K⁻¹, which yield a reduction of about 60% in conductivity between 300 and 900 K (Figure A1b). In the full expression of Xu et al. (2004) there is an additional term for pressure but, over the range of depths of interest here, this is of order 5% and is neglected. Furlong and Chapman (2013) describe the thermal conductivity of the crust by

$$K(T, z) = \frac{k_0}{[1 + b(T - 20)]} \quad (\text{A22})$$

where T is temperature in °C, k_0 and b are constants and, again, a slight dependence on pressure is neglected. Here the constants for the upper crust are used: $k_0 = 3.0$ Wm⁻¹ K⁻¹, $b = 1.5 \times 10^{-3}$ K⁻¹.

The variation of conductivity with temperature can be closely approximated by taking the appropriate average. Consider a vertical section in which internal heat production may be neglected. In the absence of heat production, the 1-D steady state heat equation may be written

$$\frac{d^2 \Theta}{dz^2} = 0, \quad (\text{A23})$$

where

$$\Theta = \int K(T') dT' \quad (\text{A24})$$

(Carslaw & Jaeger, 1959, p. 11), the solution to which is

$$T = T_0 + \frac{Qz}{K}, \quad (\text{A25})$$

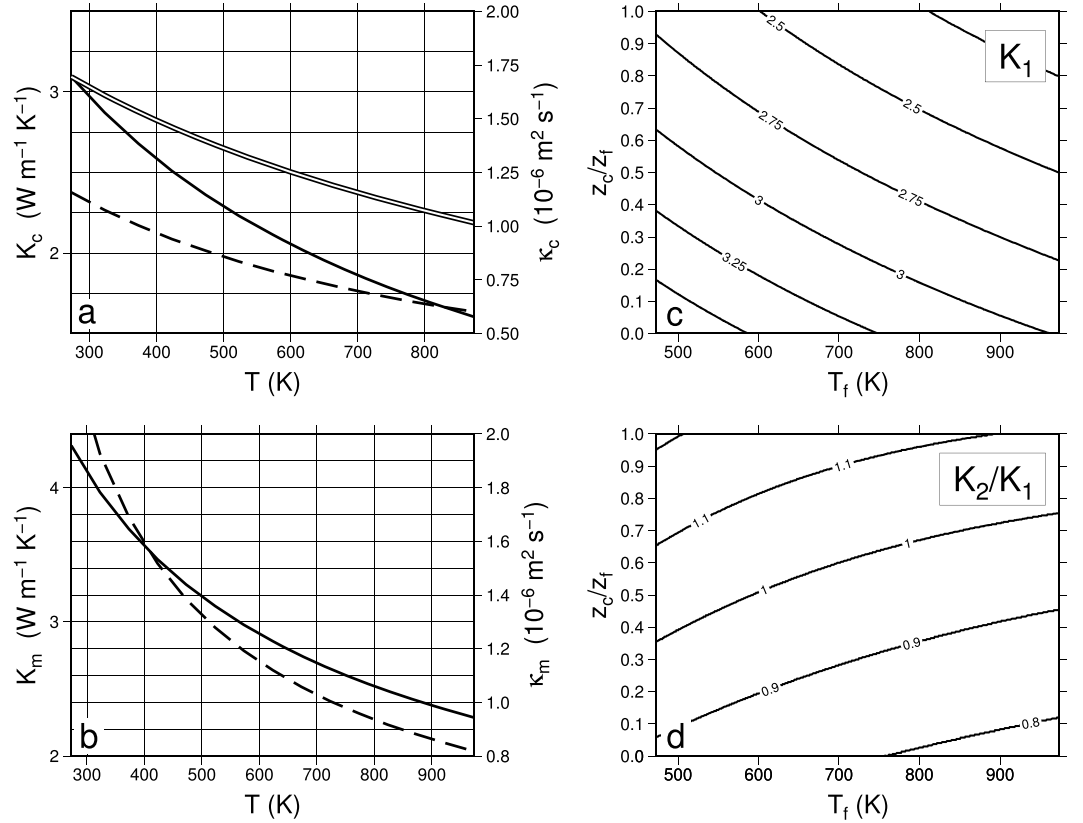


Figure A1. Variation with temperature of thermal conductivity and diffusivity in crust and mantle. (a) Variation of thermal conductivity, K_c (Furlong & Chapman, 2013) and thermal diffusivity, κ_c , of the crust (solid black and dashed lines, respectively). Double line is average conductivity (equation (A27)) for the crust, assuming a surface temperature of 273 K and temperature T at its base. (b) Same as (a) but for the mantle (Xu et al., 2004); diffusivity calculated using the expression of Berman and Aranovich (1996) for specific heat and a density of 3,300 kg/m³. (c) Average thermal conductivity, K_1 , of the upper plate as a function of temperature at the plate interface, T_f , and ratio of thickness of the crust, z_c , to depth of the interface, z_f . (d) Ratio of the thermal conductivity of the mantle at the plate interface, K_2 , (Figure 1 and equations (A3) and (A6)), to the average thermal conductivity of the upper plate.

where T_0 is the temperature on $z = 0$, Q is the heat flux, and

$$\bar{K} = \frac{1}{(T - T_0)} \int_{T_0}^T K(T') dT'. \quad (\text{A26})$$

The average conductivity for the crust between the surface, temperature T_0 , and its base, temperature T_m , is (equation (A22))

$$\bar{K}_c = \frac{k_0}{b(T_m - T_0)} \ln \left[\frac{1 + b(T_m - 20)}{1 + b(T_0 - 20)} \right] \quad (\text{A27})$$

This quantity is shown by the double line in Figure A1a. The average conductivity for a section of the mantle between temperatures T_1 and T_2 is (equation (A21))

$$\bar{K}_m = \frac{K_0 T_0^p}{(1 - p)(T_2 - T_1)} \left[T_2^{(1-p)} - T_1^{(1-p)} \right] \quad (\text{A28})$$

$$\bar{K}_m = \frac{K_0 (T_0/T_1)^p}{(1 - p)} \left[\frac{(T_2/T_1)^{(1-p)} - 1}{(T_2/T_1 - 1)} \right] \quad (\text{A29})$$

Figure A1c plots the average conductivity of the upper plate as a function of temperature on the plate interface, T_f , and the ratio, z_c/z_f , of crustal thickness to depth to the plate interface. For the relevant ranges

Table A1
Notation

Parameter	Definition	Value/Reference
a	Age of oceanic lithosphere	Myr
A	Rate of radiogenic heat production in the upper plate	$\mu\text{W}/\text{m}^3$
D	Length scale for radioactive heat production	15 km
D	Lesser of D and z_f	km
g	Acceleration due to gravity	9.8 m/s^2
K	Thermal conductivity	$\text{Wm}^{-1} \text{K}^{-1}$
K_c	Thermal conductivity of crust	equation (A22)
K_m	Thermal conductivity of mantle	equation (A21)
K_1	Average thermal conductivity of upper plate	equation (A26)
K_2	Thermal conductivity at top of lower plate	equation (A26)
L^*	Characteristic slip-weakening length (Rice, 2006, equation (23b))	equation (19)
M	Scalar moment of earthquake	N m
M_x	Maximum magnitude of earthquakes on a given interface	
$\mathcal{M}, \mathcal{M}_x$	Reduced moment of earthquake, maximum reduced moment on a given interface	equation (D4)
Q_s	Surface heat flux	mW/m^2
Q_T	$K_1 T_T / z_T$	equation (A18)
Q_0	Surface heat flux through ocean floor before it enters the trench (equations (8) and (9))	mW/m^2
Q_1	Heat flux into base of upper plate	$= Q_2 + \tau' V$
Q_2	Heat flux out of top of lower plate	equation (A4)
S	Dimensionless factor	equation (3)
t	Time	s
T^a	Temperature	$^{\circ}\text{C}$
T_f	Temperature on the plate interface at depth z_f	equation (A9)
T_T	Temperature on the plate interface at depth z_T	
u	Slip in an earthquake	m
u_x	Maximum slip in earthquakes on a given interface	m
V	Speed of convergence between plates	mm/year
V_n	Component of V perpendicular to trench	mm/year
W	Downdip width of seismogenic zone	km
x_T	Horizontal coordinate of surface above z_T	km
y	Depth below top of lower plate	km
z	Depth below surface	km
z_f	Depth of subduction interface	km
z_T	Maximum depth of thrust-faulting earthquakes on subduction interface	km
δ	Average dip of plate interface between surface and z_f	
κ	Thermal diffusivity	$10^{-6} \text{ m}^2/\text{s}$
λ	Ratio of pore fluid pressure to normal stress	
μ'	Apparent coefficient of friction	equation (1)
$\bar{\rho}$	Average density of upper plate	equation (1)
τ'	Apparent shear stress	Pa
$\bar{\tau}$	Average shear stress during an earthquake (equation (18))	Pa
χ	Fraction of plate relative motion accommodated by earthquakes (coupling of Pacheco et al., 1993; Scholz & Campos, 1995)	

^aThe Celsius scale is used; the boundary condition on temperatures at $z = 0$ (the land surface or the sea floor) is close to 0°C .

of these parameters, K_1 varies from 3.5 to 2.25 Wm⁻¹ K⁻¹. For this reason, the analyses of sections 3.2 and 3.3 use quantities that can be calculated from observations without needing to know the thermal conductivity of the upper plate. The parameter S (equation (A6)), which enters every equation in the analysis, depends on the ratio of the thermal conductivity of the mantle near the plate interface, K_2 , to average conductivity of the upper plate, K_1 . For the purposes of the present analysis, K_2 is taken to be $K_m(T_f)$; with this assumption K_2/K_1 varies little over the relevant ranges of T_f and z_c/z_f and generally lies in the range 1.0 ± 0.2 (Figure A1d). A value of 1.0 for K_2/K_1 is used in this paper.

Appendix B: Estimates of μ' From Heat Flux Profiles

This appendix applies the methods of section 3 to estimating the apparent coefficient of friction from five of the remaining profiles of heat flux considered by Gao and Wang (2014); their profile from S. Chile is not considered because all the heat flux measurements are closer than 50 km to the trench (section 2.2).

B1. Hikurangi Margin

The Hikurangi margin (Figure B1) exhibits low levels of seismicity and the maximum depth of thrust faulting is difficult to define. Based on a combination of seismic and geodetic data, Wallace et al. (2009) argue that the seismic-aseismic transition occurs at a depth of ~ 10 km north of about 40°S and deeper than 30 km south of that. The red contours in Figure B1a show the depth to the subduction interface (Williams et al., 2013), and the dashed cyan line on shows the location of the depth below which Wallace et al. (2009) infer that more than half of the plate motion occurs by stable sliding. Heat flux measurements are consistent along the margin, and show no dependence on whether or not they lie above the part of the plate boundary that is currently absorbing plate motion by steady slip (McCaffrey et al., 2008; Figure 2b).

Because of the presence of M_w 5–6 thrust-faulting earthquakes to depths of about 20 km on the subduction interface in the northern part of this margin (Figure B1a, and see Webb & Anderson, 1998), the present analysis adopts a common depth of 20 km for the maximum depth of thrust faulting along the entire margin. The best fitting value of μ' is 0.07. If uncertainties due to heat flux measurements alone are considered (Figure B1c), then $0.02 \lesssim \mu' \lesssim 0.12$; if uncertainties in heat production alone are considered (Figure B1d), $0.03 \lesssim \mu' \lesssim 0.11$. The fit is not sensitive to the choice of maximum depth of thrust-faulting earthquakes; Figure B1c shows that this range of μ' would fit the heat flux measurements equally well if a cutoff of 10 km were imposed. McCaffrey et al. (2008) favored a shear stress 20 MPa at all depths, which corresponds to μ' between 0.06 at 10 km and 0.03 at 20 km. The value chosen by Gao and Wang (2014) was 0.13.

B2. Nankai

The profile line is that of Gao and Wang (2014). z_T is taken from the downdip limit of rupture of the 1944 and 1946 $M_w \sim 8.1$ earthquakes (Baba & Cummins, 2005), which is consistent with the locking depths of 25–30 km determined geodetically for the region (Aoki & Scholz, 2003; Mazzotti et al., 2000). The age of the ocean floor beneath this profile is about 20 Myr, although some uncertainty attaches to this age due to the rapid evolution of plate boundaries in this region (see Wang, Hyndman, et al., 1995, for a discussion of this with respect to thermal modeling). Using the thermal plate model (equation (8) to estimate Q_0 for this profile yields a best fitting value of $\mu' = 0.06$ ($0.02 < \mu' < 0.11$; Figure B2b). When Q_0 is systematically varied between zero and 200 mW/m² (Figure B2c), the lowest misfit is found with $Q_0 = 110$ mW/m² and $\mu' = 0.05$. With Q_0 fixed to 110 mW/m², $0.01 < \mu' < 0.09$ (Figure B2d); if uncertainties in heat production alone are considered, $0.02 \lesssim \mu' \lesssim 0.08$ (Figure B2d).

Hamamoto et al. (2011) calculated, from a data set similar to that used here, that $\mu' \lesssim 0.1$. Yoshioka et al. (2013) showed that an apparent coefficient of friction of $\mu' \sim 0.05$ is required on the interface. The agreement between these estimates is probably misleading; as in the case of Cascadia (Figure 4), uncertainties in Q_0 and AD permit a large range in μ' : at least $0.02 \lesssim \mu' \lesssim 0.1$. Gao and Wang (2014) chose a value of $\mu' = 0.03$, as assumed by Wada and Wang (2009).

B3. Manila Trench

Figure B3 shows heat flux inferred by Chi and Reed (2008) from the depths of bottom-simulating reflectors; only estimates derived from reflectors of their qualities 1 or 2 are used. The line of the profile is close to those used by Chi and Reed (2008) and Gao and Wang (2014). Although there are many other estimates of heat flux in the data set of Chi and Reed (2008) this profile provides the best constraint on μ' . The plate interface is

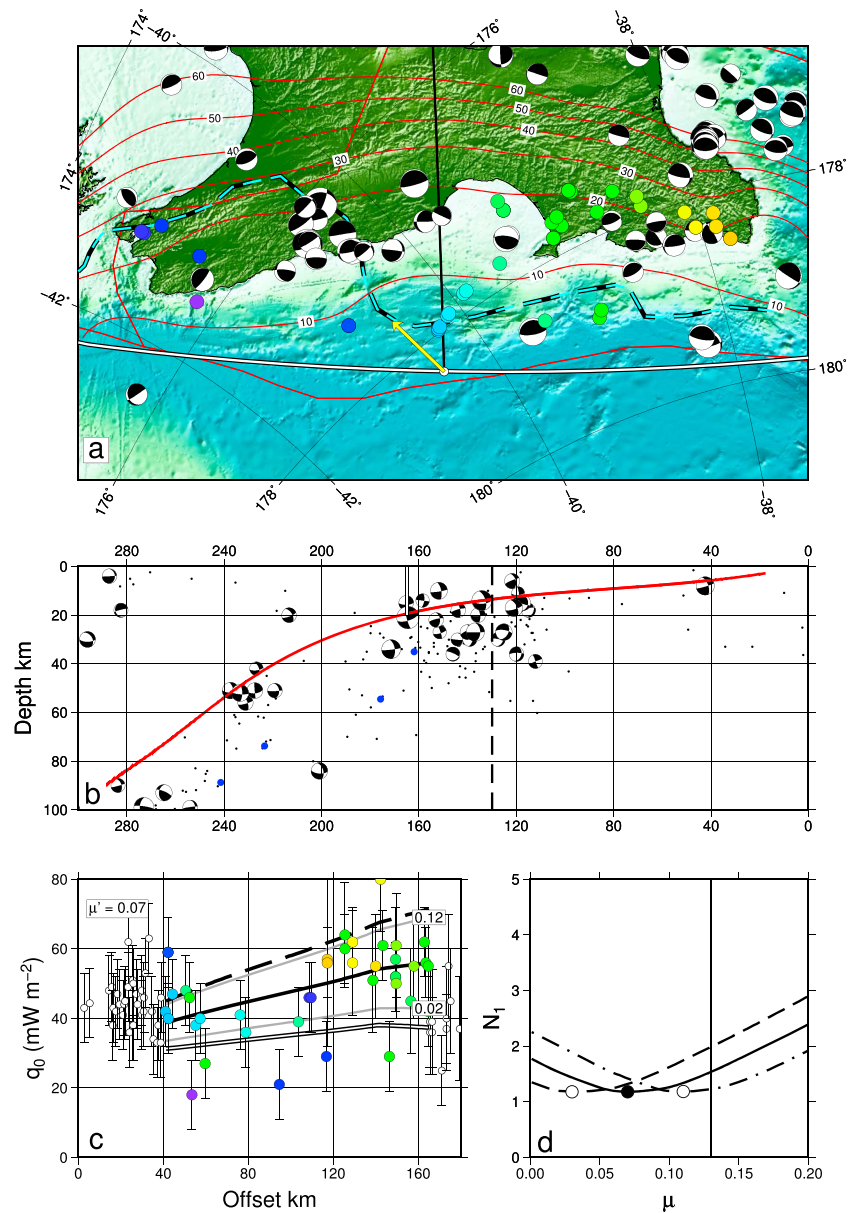


Figure B1. As in Figure 3 but for the Hikurangi margin. In panel (a) the dashed cyan line shows the 50% coupling line of Wallace et al. (2009); white line shows the small circle perpendicular to which the profiles of (b) and (c) are drawn. In (a) and (b), focal mechanisms are from Ristau (2018). In panel (c), open symbols show heat flux measurements that are excluded from the analysis, either because they are closer than 40 km to the trench, as discussed in section 2.2, or because they lie beyond the horizontal projection of the assumed maximum depth of thrust-faulting earthquakes. In panel (d), the dashed and dash-dotted lines show the variation in weighted misfit (N_1 , equation (16)) calculated with AD , respectively, at 1.5 and 0.5 times the value of 25.5 mW/m² adopted by Gao and Wang (2014).

constrained by global centroid moment tensor solutions (Ekström et al., 2012) with hypocenters determined by International Seismological Centre (2015; Figure B3b). The best fitting value of μ' is 0.06 ($0.05 < \mu' < 0.07$; Figure B3b). If uncertainties in heat production alone are considered, $0.04 \lesssim \mu' \lesssim 0.08$.

The value chosen by Gao and Wang (2014) is $\mu' \sim 0.09$. Chi and Reed (2008) used the analytical solution of Molnar and England (1990) to calculate heat flux under the assumption of no dissipative heating on the interface. They show (Chi & Reed, 2008, Figure 2) that the estimates of heat flux above the seismogenic portion of the interface lie about 15 mW/m² higher than the calculated heat fluxes, and note that a constant shear stress on the interface of 25 MPa would raise the calculated heat flux by 18 mW/m². However, their calculations assumed a dip of 8° for the interface which is likely too low. An average dip of 20° is suggested

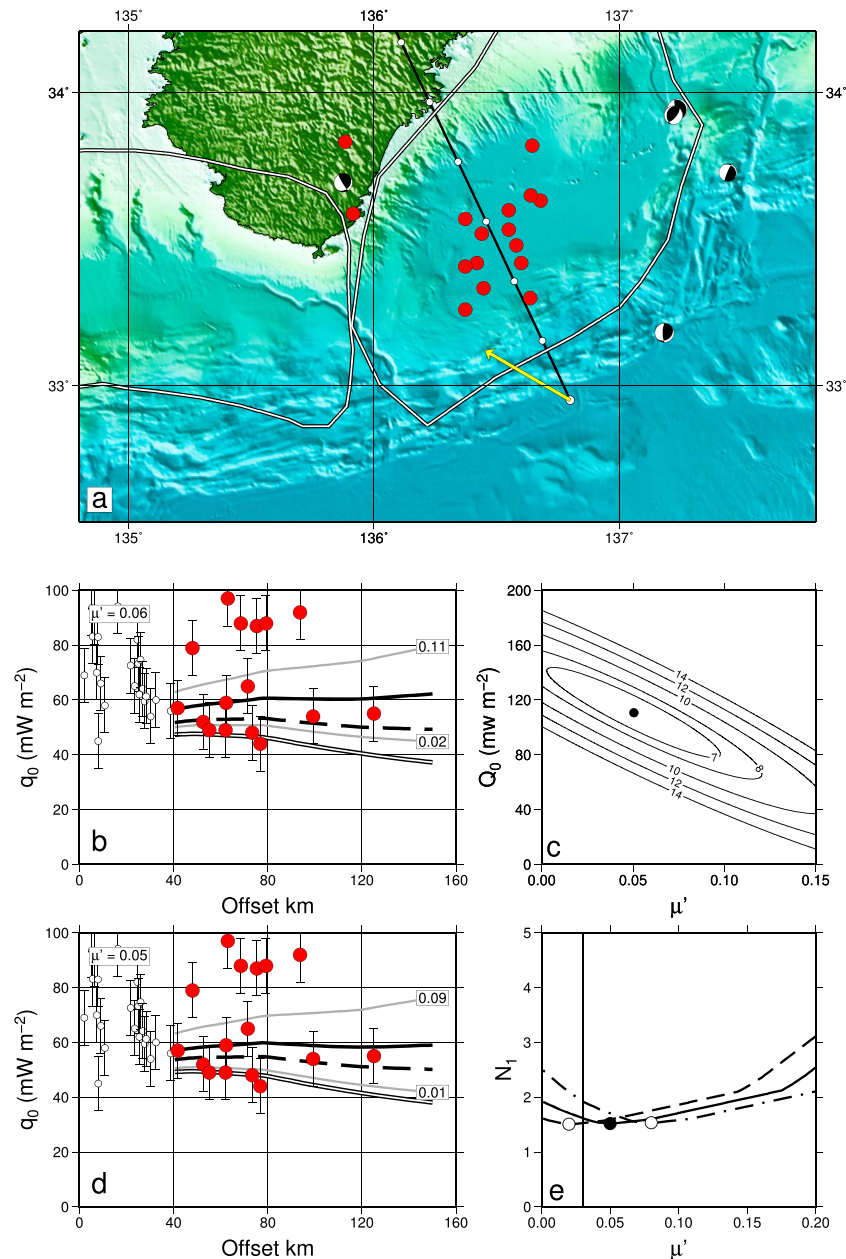


Figure B2. As in Figure 4 but for Nankai. In panel (a), white lines show estimated rupture areas of the 1944 and 1946 $M_w \sim 8.1$ earthquakes (Baba & Cummins, 2005). (b) Fit to heat flux observations with age of ocean floor taken to be 20 Myr. (c) Range of mean misfits to heat flux observations as Q_0 and μ' are varied. (d) Fit to heat flux observations with $Q_0 = 110$ mW/m², the best fitting value in (c). In panel (e), the dashed and dash-dotted lines show the variation in weighted misfit (N_1 , equation (16)) calculated with $Q_0 = 110$ mW/m² and AD , respectively, at 1.5 and 0.5 times the value of 22.5 mW/m² adopted by Gao and Wang (2014).

by the depths of thrust-faulting earthquakes (Figure B3b); this dip, with a $V_n \sim 70$ mm/year and $z_T = 35$ km, gives $S \sim 8$ hence, from equation (A13), an estimate of about 50 MPa for the shear stress on the interface required to elevate the heat flux by 15 mW/m². That shear stress is equivalent to $\mu' \sim 0.05$.

B4. N Honshu

The best fitting value of μ' is 0.05 ($0.04 < \mu' < 0.07$) (Figure B4b); the range if uncertainties in heat production alone are considered is $0.03 \lesssim \mu' \lesssim 0.08$ (Figure B4d). The value chosen by Gao and Wang (2014) is $\mu' = 0.025$. Furukawa and Uyeda (1989) concluded that the frictional stress should be lower than 20 MPa,

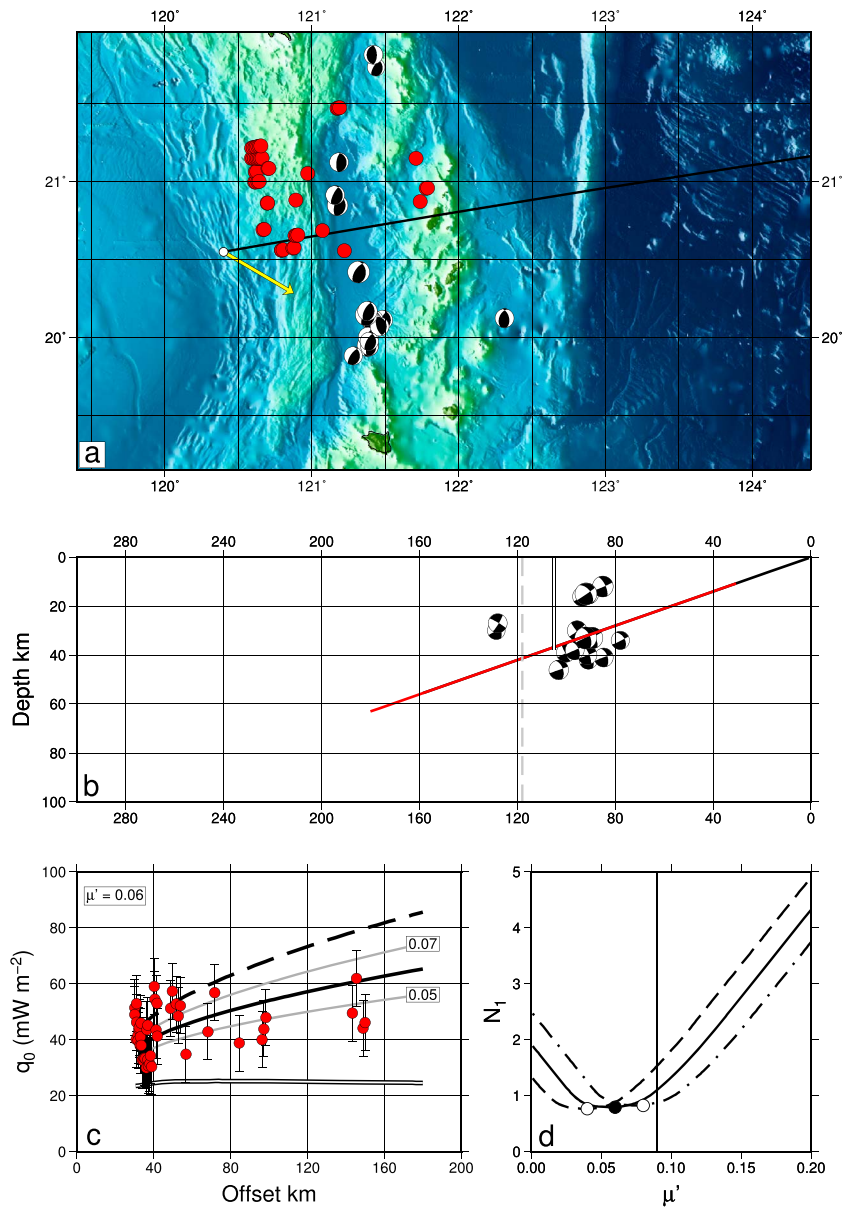


Figure B3. As in Figure B1 but for the Manila trench. In panel (b) all thrust-faulting focal mechanisms within 100 km of the profile are plotted. In panel (d), the dashed and dash-dotted lines show the variation in weighted misfit (N_1 , equation (16) calculated with AD , respectively, at 1.5 and 0.5 times the value of 19.5 mW/m^2 adopted by Gao and Wang (2014).

which corresponds to $0.03 < \mu' < 0.01$ in the depth range 20 to 60 km, similar to values assumed in several numerical modeling studies of the region (e.g., Kimura et al., 2012; Peacock & Wang, 1999; Wada & Wang, 2009).

B5. Sumatra

The profile is close to that modeled by Gao and Wang (2014); Hippchen and Hyndman (2008); Klingelhoefer et al. (2010) and Wada and Wang (2009). The best fitting value of μ' is 0.06 ($0.02 < \mu' < 0.09$; Figure B5b); if uncertainties in heat production alone are considered, $0.04 \lesssim \mu' \lesssim 0.08$ (Figure B5d). The value chosen by Gao and Wang (2014) is $\mu' = 0.03$ and they, as in the present analysis, find that $\mu' > 0.08$ is inconsistent with the heat flux. Klingelhoefer et al. (2010) carried out a finite-element calculation with no shear heating and showed (their Figure 19b) that it systematically underfits heat flux measurements within 200 km of the trench. Hippchen and Hyndman (2008) also used a 2-D finite-element model, with a frictional heating rule

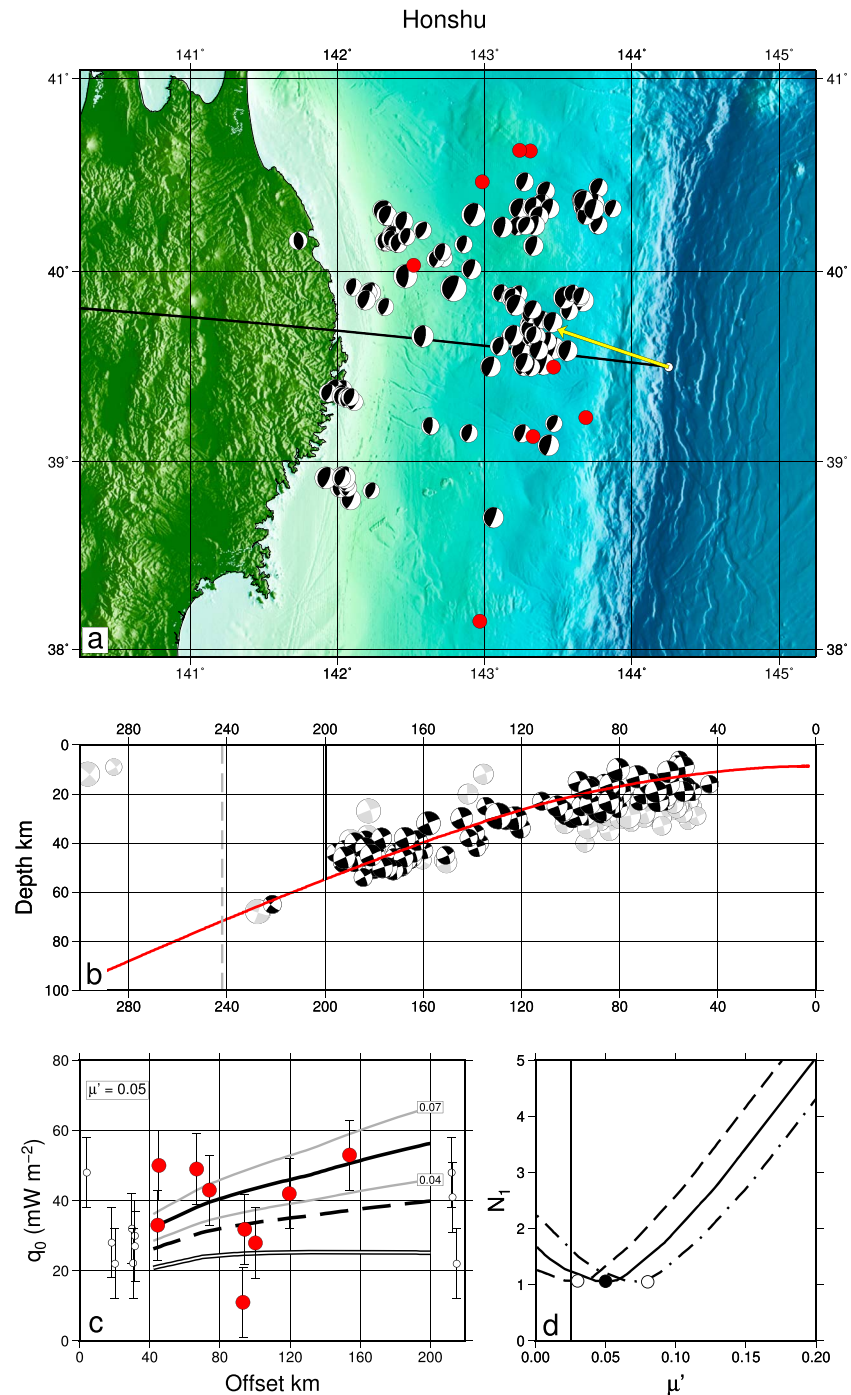


Figure B4. As Figure B1 but for northern Honshu. In panel (d), the dashed, and dot-dashed, lines show the variation in weighted misfit (N_1 , equation (16) calculated with AD, respectively, at 1.5 and 0.5 times the value of 22.5 mW/m² adopted by Gao and Wang (2014).

to a depth of 40 km, and an unspecified ductile flow rule below this depth. Their effective coefficient of friction can be estimated from their Figure 5c, in which the contribution to frictional heating to the surface heat flux is of order 5 mW/m². For this profile S (equation (A6)) is about 6, hence the contribution of dissipation to the surface heat flux is about 30 mW/m² (equation (A13)); with a convergence rate of ~ 45 mm/year, this is equivalent to a shear stress of 20 MPa, or a coefficient of friction of 0.015 at a depth of 40 km.

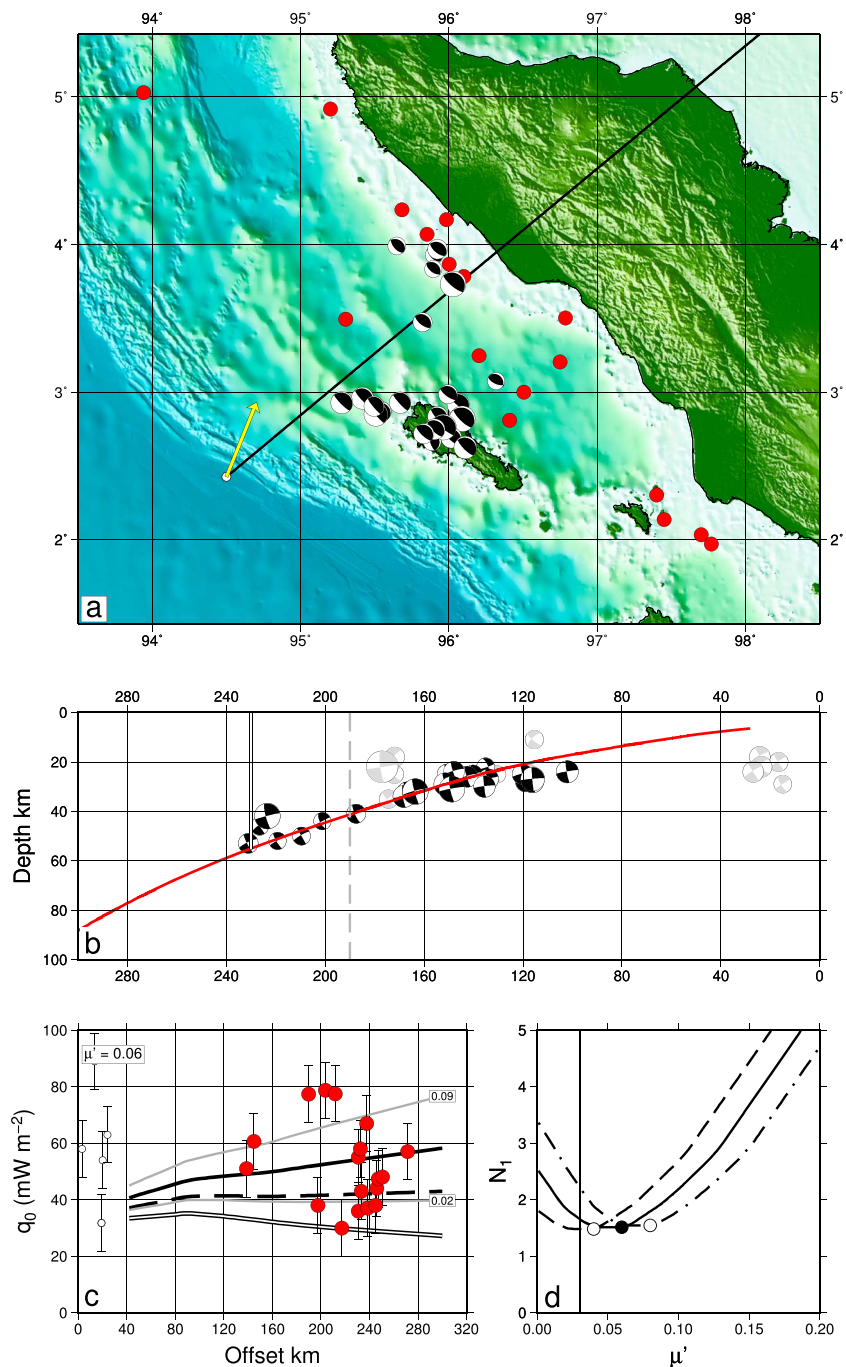


Figure B5. As in Figure B1 but for northern Sumatra. In panel (d), the dashed and dash-dotted lines show the variation in weighted misfit (N_1 , equation (16)) calculated with AD , respectively, at 1.5 and 0.5 times the value of 19.5 mW/m² adopted by Gao and Wang (2014).

Appendix C: Maximum Depths of Thrust-Faulting Earthquakes

Compilations of the maximum depth of thrust faulting on the subduction interface have been made by Heuret et al. (2011) and Hayes et al. (2012). Hayes et al. (2012) used a statistical analysis of precise hypocentral depths (International Seismological Centre, 2015) and focal mechanisms (Dziewonski et al., 1981; Ekström et al., 2012) to solve for the configuration of the subduction interfaces in most of the world's subduction zones. Then, following Pacheco et al. (1993), they identified the depth limit of thrust faulting from the 95th percentile of the distributions of depths of thrust-faulting earthquakes. Heuret et al. (2011) constructed regularly spaced

cross sections across all the major subduction zones, augmenting the data used by Hayes et al. (2012) with the hypocenters of $M \geq 7$ earthquakes from the catalog of Engdahl and Villaseñor (2002) whose hypocenters lie close to the slab, between the volcanic arc and 50 km from the trench — under the assumption that these earthquakes represent thrust faulting on the interface.

The two approaches produced estimates of the maximum depth of thrust faulting that differ by up to 20 km for the same subduction zone, with the estimates of Heuret et al. (2011) generally being deeper. Heuret et al. (2011) may have overestimated the maximum depth of thrust faulting earthquakes by using the $M \geq 7$ earthquakes from the catalog of Engdahl and Villaseñor (2002) whose focal mechanisms are unknown. The procedure used here plots the focal mechanisms of the global centroid moment tensor catalog between 1976 and 2013 (Dziwonski et al., 1981; Ekström et al., 2012), with hypocentral coordinates as given by International Seismological Centre (2015), on cross sections drawn perpendicular to the trench. The locations of sections are those of Heuret and coworkers (Lallemand et al., 2005; Heuret et al., 2017). Earthquakes are assigned to the interface if they meet the following criteria:

1. They satisfy the quality constraints of Frohlich and Davis (1999).
2. Their epicenters are within 100 km of the profile.
3. One fault plane dips away from the trench and has a dip within 20° of the dip of the slab.
4. That plane has a rake between 60° and 120° .
5. The hypocenter lies within 10 km of the depth of the slab.

For profiles in which fewer than 20 such events could be identified, or z_T could not be reliably defined, constraint (1) was removed, constraint (2) was relaxed to 200 km, constraint (3) to 30° , and constraint (4) to the rake's lying between 45° and 135° . If z_T still could not be reliably defined, the profile was excluded from the analysis.

On practically all of the sections that meet these criteria, there is an abrupt cutoff, x_T , in the horizontal location of thrust-faulting earthquakes with distance from the trench (usually over 5 to 10 km); with x_T between 100 and 300 km, this corresponds to a fractional uncertainty of a few percent. The maximum depth, z_T , of thrust-faulting earthquakes is set to be the depth of the slab at that horizontal coordinate, determined by Hayes et al. (2012). The cross sections are shown in the supporting information.

Appendix D: Apparent Coefficient of Friction for Slip on A Shear Zone With Thermal Pressurization During Earthquakes

Consider an area, Σ , of subduction interface across which slip at a rate V is accommodated by earthquakes obeying a Gutenberg-Richter relation, here written in terms of the moment, M , and the frequency, N , of earthquakes having moment greater than M :

$$N = \alpha M^{-\beta} \quad (D1)$$

The time interval of interest is the time required for heat to diffuse through the upper plate, which is sufficiently long that equation (D1) may be assumed to exhibit no time dependence.

Hereinafter, the shear modulus is taken to be constant, and the symbol \mathcal{M} is used to denote the reduced moment: moment divided by shear modulus. If all the convergence across the plate interface takes place in earthquakes whose maximum reduced moment is \mathcal{M}_x then

$$\Sigma V = - \int_0^{\mathcal{M}_x} \mathcal{M} \frac{dN}{d\mathcal{M}} d\mathcal{M} \quad (D2)$$

$$\Sigma V = \mathcal{M}_x^{(1-\beta)} \frac{\alpha\beta}{1-\beta} \quad (D3)$$

(Brune, 1968; Molnar, 1979).

The relation between the slip in and the reduced moment of each earthquake is taken to be

$$\mathcal{M} = \Delta \Sigma u = \gamma u^3, \quad (D4)$$

where it has been assumed that the slip, u , is proportional to the square root of the area, $\Delta\Sigma$, over which slip occurs (e.g., Wells & Coppersmith, 1994).

The total rate of heat released by all earthquakes taking place on the surface Σ is

$$Q = - \int_0^{u_x} \bar{\tau}(u) \Delta\Sigma(u) u \frac{dN}{du} du \quad (D5)$$

$$= \frac{3\Sigma V(1-\beta)}{u_x^{3(1-\beta)}} \int_0^{u_x} \bar{\tau}(u) u^{(2-3\beta)} du, \quad (D6)$$

where u_x is the greatest slip in an earthquake on the interface; $\bar{\tau}(u)$ is given by equation (18) (after Rice, 2006, equation (30)) and

$$\frac{dN}{du} = -3\alpha\beta\gamma^{-\beta} u^{(-1-3\beta)}, \quad (D7)$$

$$\alpha\beta = \frac{\Sigma V(1-\beta)}{\mathcal{M}_x^{(1-\beta)}} = \frac{\Sigma V(1-\beta)}{\gamma^{(1-\beta)} u_x^{3(1-\beta)}}. \quad (D8)$$

The apparent shear stress on the interface, τ' , is $Q/(\Sigma V)$

$$\tau' = \frac{3(1-\beta)}{u_x^{3(1-\beta)}} \int_0^{u_x} \bar{\tau}(u) u^{(2-3\beta)} du. \quad (D9)$$

Substituting $\bar{\tau}(u)$ from equation (18), we obtain

$$\mu' = \frac{\tau'}{\sigma_n} = \mu_0 (1 - \lambda) \frac{3(1-\beta)}{u_x^{3(1-\beta)}} \int_0^{u_x} \frac{L^*}{u} \left[\exp\left(\frac{u}{L^*}\right) \operatorname{erfc}\left(\sqrt{\frac{u}{L^*}}\right) + 2\sqrt{\frac{u}{\pi L^*}} - 1 \right] u^{(2-3\beta)} du. \quad (D10)$$

Acknowledgments

The heat flux data are those compiled by Gao and Wang (2014), from publications cited in that source. I am grateful to Wu-Cheng Chi, Xiang Gao, and Kelin Wang for sharing their data. I thank N. Brantut and an anonymous reviewer for their insightful comments. J. Hawthorne, J. Jackson, R. Katz, C. Marone, P. Molnar, and A. Smye also gave helpful comments. This work was supported by the Natural Environment Research Council (NERC) and the Economic and Social Research Council through grant NE/J02001X/1. Most of the figures were prepared using the GMT package (Wessel & Smith, 2013).

References

- Abers, G. A., Van Keken, P. E., & Hacker, B. R. (2017). The cold and relatively dry nature of mantle forearcs in subduction zones. *Nature Geoscience*, 40, 1–5.
- Abramowitz, M., & Stegun, I. A. (Eds.). (1970). *Handbook of mathematical functions* (9th ed.). New York: Dover.
- Andrews, D. J., & Ben-Zion Y. (1997). Wrinkle-like slip pulse on a fault between different materials. *Journal Of Geophysical Research*, 102(B1), 553–571.
- Aoki, Y., & Scholz, C. H. (2003). Interseismic deformation at the Nankai subduction zone and the Median Tectonic Line, southwest Japan. *Journal of Geophysical Research*, 108(B10), 2470. <https://doi.org/10.1029/2003JB002441>
- Argus, D. F., Gordon, R. G., & Demets, C. (2011). Geologically current motion of 56 plates relative to the no-net-rotation reference frame. *Geochemistry Geophysics Geosystems*, 12, Q11001. <https://doi.org/10.1029/2011GC003751>
- Baba, T., & Cummins, P. (2005). Contiguous rupture areas of two Nankai Trough earthquakes revealed by high-resolution tsunami waveform inversion. *Geophysical Research Letters*, 32, L08305. <https://doi.org/10.1029/2004GL022320>
- Barr, T. D., & Dahlen, F. A. (1989). Brittle frictional mountain building 2. Thermal structure and heat-budget. *Journal Geophysical Research*, 94, 3923–3947.
- Beeler, N. M., Tullis, T. E., & Goldsby, D. L. (2008). Constitutive relationships and physical basis of fault strength due to flash heating. *Journal of Geophysical Research*, 113, B01401. <https://doi.org/10.1029/2007JB004988>
- Ben-Zion, Y., & Ampuero, J.-P. (2009). Seismic radiation from regions sustaining material damage. *Geophysical Journal International*, 178, 1351–1356. <https://doi.org/10.1111/j.1365-246X.2009.04285.x>
- Berman, R., & Aranovich, L. (1996). Optimized standard state and solution properties of minerals: 1. Model calibration for olivine, orthopyroxene, cordierite, garnet, and ilmenite in the system FeO–MgO–CaO–Al₂O₃–TiO₂–SiO₂. *Contrib. Mineralogy and Petrology*, 126, 1–24.
- Birch, F., Roy, R., & Decker, E. (1968). Heat flow and thermal history in New York and New England. In E. Zen, et al. (Eds.), *Studies of Appalachian geology: Northern and maritime* (pp. 437–451).
- Blackwell, D. D. (1971). The thermal structure of the continental crust. In J. G. Heacock (Ed.), *The structure and physical properties of the Earth's crust*, *Geophysical Monograph Series* (Vol. 14, pp. 169–184). Washington: American Geophysical Union.
- Blanpied, M. L., Lockner, D. A., & Byerlee, J. D. (1991). Fault stability inferred from granite sliding experiments at hydrothermal conditions. *Geophysical Research Letters*, 18(4), 609–612.
- Blanpied, M. L., Lockner, D. A., & Byerlee, J. D. (1995). Frictional slip of granite at hydrothermal conditions. *Journal of Geophysical Research*, 100(B7), 13,045–13,064.
- Bletery, Q., Thomas, A. M., Rempel, A. W., & Hardebeck, J. L. (2017). Imaging shear strength along subduction faults. *Geophysical Research Letters*, 44, 11,329–11,339. <https://doi.org/10.1002/2017GL075501>
- Bletery, Q., Thomas, A. M., Rempel, A. W., Karlstrom, L., Sladen, A., & De Barros, L. (2016). Mega-earthquakes rupture flat megathrusts. *Science*, 354(6315), 1027–1031.
- Brantut, N., & Platt, J. D. (2017). Dynamic weakening and the depth dependence of earthquake faulting. In M. Y. Thomas, T. M. Mitchell, & H. S. Bhat (Eds.), *Fault zone dynamic processes*, *Geophysical Monograph* (Vol. 227, pp. 171–194). AGU & John Wiley.
- Brune, J. N. (1968). Seismic moment, seismicity and rate of slip along major fault zones. *Journal of Geophysical Research*, 73, 777–784.

- Byerlee, J. (1978). Friction of rocks. *Pure and Applied Geophysics*, 116, 615–626.
- Carpenter, B. M., Saffer, D. M., & Marone, C. (2012). Frictional properties and sliding stability of the San Andreas Fault from deep drill core. *Geology*, 40(8), 759–762.
- Carslaw, H. S., & Jaeger, J. C. (1959). *Conduction of heat in solids* (2nd ed.). Oxford: University Press.
- Cattin, R., Lyon-Caen, H., & Chéry, J. (1997). Quantification of interplate coupling in subduction zones and forearc topography. *Geophysical Research Letters*, 24, 1563–1566.
- Chi, W. C., & Reed, D. L. (2008). Evolution of shallow, crustal thermal structure from subduction to collision: An example from Taiwan. *Geological Society of America Bulletin*, 120, 679–690. <https://doi.org/10.1130/B26210.1>
- Cloos, M., & Shreve, R. (1988). Subduction-channel model of prism accretion, melange formation, sediment subduction, and subduction erosion at convergent plate margins: 1. Background and description. *Pure Applied Geophysics*, 128, 455–500.
- Colletini, C., Niemeijer, A., Viti, C., & Marone, C. (2009). Fault zone fabric and fault weakness. *Nature*, 462, 907–910.
- Cozzens, B. D., & Spinelli, G. A. (2012). A wider seismogenic zone at Cascadia due to fluid circulation in subducting oceanic crust. *Geology*, 40(10), 899–902.
- Cubas, N., Avouac, J. P., Leroy, Y. M., & Pons, A. (2013). Low friction along the high slip patch of the 2011 Mw 9.0 Tohoku-Oki earthquake required from the wedge structure and extensional splay faults. *Geophysical Research Letters*, 40, 4231–4237. <https://doi.org/10.1002/grl.50682>
- Curran, P. A. (2015). Monte Carlo error analyses of Spearman's rank test. <https://arxiv.org/abs/1411.3816v2>
- Dahlen, F. A. (1990). Critical taper model of fold-and-thrust belts and accretionary wedges. *Annual Review and Earth Planetary Sciences*, 18, 55–99.
- Davis, D., Suppe, J., & Dahlen, F. A. (1983). Mechanics of fold-and-thrust belts and accretionary wedges. *Journal of Geophysical Research*, 88(B2), 1153–1172.
- den Hartog, S. A. M., Niemeijer, A. R., & Spiers, C. J. (2012). New constraints on megathrust slip stability under subduction zone P–T conditions. *Earth and Planetary Science Letters*, 353–354, 240–252.
- den Hartog, S. A. M., Niemeijer, A. R., & Spiers, C. J. (2013). Friction on subduction megathrust faults: Beyond the illite–muscovite transition. *Earth and Planetary Science Letters*, 373, 8–19.
- Di Toro, G., Hirose, T., Nielsen, S., Pennacchioni, G., & Shimamoto, T. (2006). Natural and experimental evidence of melt lubrication of faults during earthquakes. *Science*, 311(5761), 647–649.
- Dielforder, A. (2017). Constraining the strength of megathrusts from fault geometries and application to the Alpine collision zone. *Earth and Planetary Science Letters*, 474, 49–58.
- Dziewonski, A. M., Chou, T.-A., & Woodhouse, J. H. (1981). Determination of earthquake source parameters from waveform data for studies of global and regional seismicity. *Journal Geophysical Research*, 86, 2825–2852.
- Ekström, G., Nettles, M., & Dziewonski, A. (2012). The Global CMT Project 2004–2010: Centroid-moment tensors for 13,017 earthquakes. *Physics of the Earth and Planetary Interiors*, 200–201, 1–9.
- Emmerson, B., & McKenzie, D. (2007). Thermal structure and seismicity of subducting lithosphere. *Physics of the Earth Planetary Interiors*, 163, 191–208.
- Engdahl, E. R., & Villaseñor, A. (2002). Global Seismicity: 1900–1999. In W. H. K. Lee, P. Jennings, H. Kanamori, & C. Kisslinger (Eds.), *IASPEI handbook of earthquake and engineering seismology, Part A* (pp. 665–690).
- England, P., LeFort, P., Molnar, P., & Pêcher, A. (1992). Heat sources for Tertiary metamorphism and anatexis in the Annapurna-Manaslu region central Nepal. *Journal of Geophysical Research*, 97, 2107–2128.
- Fagereng, A., & den Hartog, S. A. M. (2016). Subduction megathrust creep governed by pressure solution and frictional–viscous flow. *Nature Publishing Group*, 10, 51–57.
- Fagereng, A., & Ellis, S. (2009). On factors controlling the depth of interseismic coupling on the Hikurangi subduction interface, New Zealand. *Earth and Planetary Science Letters*, 278, 120–130.
- Fagereng, A., & Sibson, R. H. (2010). Melange rheology and seismic style. *Geology*, 38, 751–754.
- Frohlich, C., & Davis, S. (1999). How well constrained are well-constrained T, B, and P axes in moment tensor catalogs. *Journal of Geophysical Research*, 104, 4901–4910.
- Fulton, P. M., Brodsky, E. E., Kano, Y., Mori, J., Chester, F., Ishikawa, T., et al. (2013). Low coseismic friction on the Tohoku-Oki fault determined from temperature measurements. *Science*, 342, 1214–1217.
- Furlong, K. P., & Chapman, D. S. (1987). Crustal heterogeneities and the thermal structure of the continental crust. *Geophysical Research Letters*, 14(3), 314–317.
- Furlong, K. P., & Chapman, D. S. (2013). Heat flow, heat generation, and the thermal state of the lithosphere. *Annual Review of Earth and Planetary Sciences*, 41, 385–410.
- Furukawa, Y., & Uyeda, S. (1989). Thermal state under the Tohoku arc with consideration of crustal heat generation. *Tectonophysics*, 164(2), 175–187.
- Gao, X., & Wang, K. (2014). Strength of stick-slip and creeping subduction megathrusts from heat flow observations. *Science*, 345, 1038–1041.
- Goldsby, D. L., & Tullis, T. E. (2011). Flash heating leads to low frictional strength of crustal rocks at earthquake slip rates. *Science*, 334, 216–218.
- Graham, C., & England, P. (1975). Thermal regimes and regional metamorphism in the vicinity of overthrust faults: An example of shear heating and inverted metamorphic zonation from southern California. *Earth and Planetary Science Letters*, 31, 142–152.
- Hamamoto, H., Yamano, M., Goto, S., Kinoshita, M., Fujino, K., & Wang, K. (2011). Heat flow distribution and thermal structure of the Nankai subduction zone off the Kii Peninsula. *Geochemistry, Geophysics, Geosystems*, 12, Q0AD20. <https://doi.org/10.1029/2011GC003623>
- Hardebeck, J. L., & Loveless, J. P. (2017). Creeping subduction zones are weaker than locked subduction zones. *Nature Geoscience*, 11, 60–64.
- Hass, B., & Harris, R. N. (2016). Heat flow along the Costa Rica Seismogenesis Project drilling transect: Implications for hydrothermal and seismic processes. *Geochemistry, Geophysics, Geosystems*, 17, 2110–2127. <https://doi.org/10.1002/2016GC006314>
- Hayes, G. P., Wald, D. J., & Johnson, R. L. (2012). Slab1.0: A three-dimensional model of global subduction zone geometries. *Journal of Geophysical Research*, 117, B01302. <https://doi.org/10.1029/2011JB008524>
- Heuret, A., Conrad, C. P., Funicello, F., Lallemand, S., & Sandri, L. (2012). Relation between subduction megathrust earthquakes, trench sediment thickness and upper plate strain. *Geophysical Research Letters*, 39, L05304. <https://doi.org/10.1029/2011GL050712>
- Heuret, A., Lallemand, S., Funicello, F., Piromallo, C., & Faccenna, C. (2011). Physical characteristics of subduction interface type seismogenic zones revisited. *Geochemistry, Geophysics, Geosystems*, 12, Q01004. <https://doi.org/10.1029/2010GC003230>
- Heuret, A., Losq, J., & Lallemand, S. (2017). Submap: A tool for mapping subduction zones. Retrieved from <http://submap.gm.univ-montp2.fr/index.php>

- Hippchen, S., & Hyndman, R. D. (2008). Thermal and structural models of the Sumatra subduction zone: Implications for the megathrust seismogenic zone. *Journal of Geophysical Research*, 113, B12103. <https://doi.org/10.1029/2008JB005698>
- Hutnak, M., Fisher, A. T., Zühlsdorff, L., Spiess, V., Stauffer, P. H., & Gable, C. W. (2006). Hydrothermal recharge and discharge guided by basement outcrops on 0.7–3.6 Ma seafloor east of the Juan de Fuca Ridge: Observations and numerical models. *Geochemistry, Geophysics, Geosystems*, 7, Q07002. <https://doi.org/10.1029/2006GC001242>
- Hyndman, R. D., & Wang, K. (1993). Thermal constraints on the zone of major thrust earthquake failure: The Cascadia subduction zone. *Journal of Geophysical Research*, 98, 2039–2060.
- Hyndman, R. D., Wang, K., & Yamano, M. (1995). Thermal constraints on the seismogenic portion of the southwestern Japan subduction thrust. *Journal of Geophysical Research*, 100, 15,373–15,392.
- Ikari, M. J., Saffer, D. M., & Marone, C. (2009). Frictional and hydrologic properties of clay-rich fault gouge. *Journal of Geophysical Research*, 114, B05409. <https://doi.org/10.1029/2008JB006089>
- International Seismological Centre (2015). EHB Bulletin, Int. Seis. Cent., Thatcham, United Kingdom. Retrieved from <http://www.isc.ac.uk>
- Jarrard, R. D. (1986). Relations among subduction parameters. *Reviews of Geophysics*, 24, 217–284.
- Jaupart, C., & Mareschal, J.-C. (2011). *Heat Generation and Transport in the Earth* (464 pp.). Cambridge University Press.
- Kano, Y., Mori, J., Fujio, I., Ito, H., Yanagidani, T., Nakao, S., & Ma, K.-F. (2006). Heat Signature on the Chelungpu fault associated with the 1999 Chi-Chi, Taiwan earthquake. *Geophysical Research Letters*, 33, L14306. <https://doi.org/10.1029/2006GL026733>
- Kao, H., & Chen, W.-P. (1991). Earthquakes along the Ryukyu-Kyushu Arc: Strain segmentation, lateral compression, and the thermomechanical state of the plate interface. *Journal of Geophysical Research*, 96(B13), 21,443–21,485.
- Kelleher, J., Savino, J., Rowlett, H., & McCann, W. (1974). Why and where great thrust earthquakes occur along island arcs. *Journal of Geophysical Research*, 79, 4889–4899.
- Kimura, G., Hina, S., Hamada, Y., Kameda, J., Tsuji, T., Kinoshita, M., & Yamaguchi, A. (2012). Runaway slip to the trench due to rupture of highly pressurized megathrust beneath the middle trench slope. The tsunamigenesis of the 2011 Tohoku earthquake off the east coast of northern Japan. *Earth and Planetary Science Letters*, 339–340(C), 32–45.
- Klingelhoefer, F., Gutscher, M. A., Ladage, S., Dessa, J.-X., Graindorge, D., Franke, D., et al. (2010). Limits of the seismogenic zone in the epicentral region of the 26 December 2004 great Sumatra-Andaman earthquake: Results from seismic refraction and wide-angle reflection surveys and thermal modeling. *Journal of Geophysical Research*, 115, B01304. <https://doi.org/10.1029/2009JB006569>
- Lachenbruch, A. H. (1980). Frictional heating, fluid pressure, and the resistance to fault motion. *Journal of Geophysical Research*, 85, 6097–6112.
- Lallemand, S., Heuret, A., & Boutelier, D. (2005). On the relationships between slab dip, back-arc stress, upper plate absolute motion, and crustal nature in subduction zones. *Geochemistry, Geophysics, Geosystems*, 6, Q09006. <https://doi.org/10.1029/2005GC000917>
- Lamb, S. (2006). Shear stresses on megathrusts: Implications for mountain building behind subduction zones. *Journal of Geophysical Research*, 111, B07401. <https://doi.org/10.1029/2005JB003916>
- Lay, T., Kanamori, H., Ammon, C. J., Koper, K. D., Hutko, A. R., Ye, L., et al. (2012). Depth-varying rupture properties of subduction zone megathrust faults. *Journal of Geophysical Research*, 117, B04311. <https://doi.org/10.1029/2011JB009133>
- Lockner, D. A., Morrow, C., Moore, D., & Hickman, S. (2011). Low strength of deep San Andreas fault gouge from SAFOD core. *Nature*, 472(7341), 82–85.
- Lomnitz-Adler, J. (1991). Model for steady-state friction. *Journal of Geophysical Research*, 96(B4), 6121–6131.
- Loveless, J. P., & Meade, B. J. (2016). Two decades of spatiotemporal variations in subduction zone coupling offshore Japan. *Earth and Planetary Science Letters*, 436, 19–30.
- Lowell, R. P., Rona, P. A., & Von Herzen, R. P. (1995). Seafloor hydrothermal systems. *Journal of Geophysical Research*, 100(B1), 327–352.
- McCaffrey, R. (2008). Global frequency of magnitude 9 earthquakes. *Geology*, 36, 263.
- McKenzie, D., Jackson, J., & Priestley, K. (2005). Thermal structure of oceanic and continental lithosphere. *Earth and Planetary Science Letters*, 233, 337–349.
- Marsan, D., Bouchon, M., Gardonio, B., Perfettini, H., Socquet, A., & Enescu, B. (2017). Change in seismicity along the Japan trench, 1990–2011, and its relationship with seismic coupling. *Journal of Geophysical Research: Solid Earth*, 122, 4645–4659. <https://doi.org/10.1002/2016JB013715>
- Marzocchi, W., Sandri, L., Heuret, A., & Funicello, F. (2016). Where giant earthquakes may come. *Journal of Geophysical Research*, 121, 7322–7336. <https://doi.org/10.1002/2016JB013054>
- Mavrommatis, A. P., Segall, P., Uchida, N., & Johnson, K. M. (2015). Long-term acceleration of aseismic slip preceding the Mw 9 Tohoku-oki earthquake: Constraints from repeating earthquakes. *Geophysical Research Letters*, 42, 9717–9725. <https://doi.org/10.1002/2015GL066069>
- Mazzotti, S., Pichon, X. L., Henry, P., & Miyazaki, S. (2000). Full interseismic locking of the Nankai and Japan-West Kurile subduction zones: An analysis of uniform elastic strain accumulation in Japan constrained by permanent GPS. *Journal of Geophysical Research*, 105, 13,159–13,177.
- McCaffrey, R., Wallace, L., & Beavan, J. (2008). Slow slip and frictional transition at low temperature at the Hikurangi subduction zone. *Nature GeoScience*, 1, 316–320.
- Molnar, P. (1979). Earthquake recurrence intervals and plate tectonics. *Bulletin of the Seismological Society of America*, 69, 115–133.
- Molnar, P., & England, P. (1990). Temperatures, heat flux, and frictional stress near major thrust faults. *Journal of Geophysical Research*, 95, 4833–4856.
- Molnar, P., & England, P. (1995). Temperatures in zones of steady-state underthrusting of young oceanic lithosphere. *Earth and Planetary Science Letters*, 131, 57–70.
- Molnar, P., Freedman, A., & Shih, J. S. (1979). Lengths of intermediate and deep seismic zones and temperatures in downgoing slabs of lithosphere. *Geophysical Journal of the Royal Astronomical Society*, 56, 41–54.
- Nielsen, S., Spagnuolo, E., Smith, S. A. F., Violay, M., Di Toro, G., & Bistacchi, A. (2016). Scaling in natural and laboratory earthquakes. *Geophysical Research Letters*, 43, 1504–1510. <https://doi.org/10.1002/2015GL067490>
- Oleskevich, D., Hyndman, R., & Wang, K. (1999). The updip and downdip limits to great 1352 subduction earthquakes: Thermal and structural models of Cascadia, south Alaska, SW 1353 Japan, and Chile. *Journal of Geophysical Research*, 104, 14,965–14,992.
- Pacheco, J. F., Sykes, L. R., & Scholz, C. H. (1993). Nature of seismic coupling along simple plate boundaries of the subduction type. *Journal of Geophysical Research*, 98, 14,133–14,159.
- Parsons, B., & Sclater, J. G. (1977). An analysis of the variation of ocean floor bathymetry and heat flow with age. *Journal of Geophysical Research*, 82, 802–827.
- Peacock, S. M. (1992). Blueschist-facies metamorphism, shear heating, and P-T-t paths in subduction shear zones. *Journal of Geophysical Research*, 97, 17,693–17,707.

- Peacock, S. M., & Wang, K. (1999). Seismic consequences of warm versus cool subduction metamorphism: Examples from Southwest and Northeast Japan. *Science*, 286(5441), 937–939.
- Penniston-Dorland, S. C., Kohn, M. J., & Manning, C. E. (2015). The global range of subduction zone thermal structures from exhumed blueschists and eclogites: Rocks are hotter than models. *Earth and Planetary Science Letters*, 428, 243–254.
- Phrampus, B. J., Harris, R. N., & Trehu, A. M. (2017). Heat flow bounds over the Cascadia margin derived from bottom simulating reflectors and implications for thermal models of subduction. *Geochemistry, Geophysics, Geosystems*, 18, 3309–3326. <https://doi.org/10.1002/2017GC007077>
- Platt, J. D., Brantut, N., & Rice, J. R. (2015). Strain localization driven by thermal decomposition during seismic shear. *Journal Of Geophysical Research: Solid Earth*, 120, 4405–4433. <https://doi.org/10.1002/2014JB011493>
- Press, W., Teukolsky, S., Vetterling, W., & Flannery, B. (1992). *Numerical recipes: The art of scientific computing* (2nd ed.). Cambridge: Cambridge University Press.
- Rempel, A. W., & Rice, J. R. (2006). Thermal pressurization and onset of melting in fault zones. *Journal of Geophysical Research*, 111, B09314. <https://doi.org/10.1029/2006JB004314>
- Rice, J. R. (1992). Fault stress states, pore pressure distributions, and the weakness of the San Andreas Fault. In B. Evans, & T.-F. Wong (Eds.), *Fault mechanics and the transport properties of rocks: A Festschrift in honor of W. F. Brace* (pp. 475–503).
- Rice, J. R. (2006). Heating and weakening of faults during earthquake slip. *Journal of Geophysical Research*, 111, B05311. <https://doi.org/10.1029/2005JB004006>
- Rice, J. R. (2017). Heating, weakening and shear localization in earthquake rupture. *Philosophical Transactions of the Royal Society A: Mathematical, Physical and Engineering Sciences*, 375, 20160015. <https://doi.org/10.1098/rsta.2016.0015>
- Ristau, J. (2018). Geonet moment tensor catalogue. Retrieved from <https://github.com/GeoNet/data/tree/master/moment-tensor>
- Rong, Y., Jackson, D. D., Magistrale, H., & Goldfinger, C. (2014). Magnitude limits of subduction zone earthquakes. *Bulletin of the Seismological Society of America*, 104(5), 2359–2377.
- Ruff, L., & Kanamori, H. (1980). Seismicity and the subduction process. *Physic of the Earth and Planetary Interiors*, 23, 240–252.
- Ruff, L. (1989). Do trench sediments affect great earthquake occurrence in subduction zones? *Pure and Applied Geophysics*, 129, 263–282.
- Saffer, D. M. (2014). The permeability of active subduction plate boundary faults. *Geofluids*, 15, 193–215.
- Saffer, D. M., & Tobin, H. J. (2011). Hydrogeology and mechanics of subduction zone forearcs: Fluid flow and pore pressure. *Annual Review Of Earth And Planetary Sciences*, 39(1), 157–186.
- Schellart, W. P., & Rawlinson, N. (2013). Global correlations between maximum magnitudes of subduction zone interface thrust earthquakes and physical parameters of subduction zones. *Physics of the Earth and Planetary Interiors*, 225, 41–67.
- Schmalzle, G. M., McCaffrey, R., & Creager, K. C. (2014). Central Cascadia subduction zone creep. *Geochemistry, Geophysics, Geosystem*, 15, 1515–1532. <https://doi.org/10.1002/2013GC005172>
- Scholz, C. H. (1998). Earthquakes and friction laws. *Nature*, 391, 37–42.
- Scholz, C. H., & Campos, J. (1995). On the mechanism of seismic decoupling and back-arc spreading at subduction zones. *Journal of Geophysical Research*, 100, 22,103–22,115.
- Scholz, C. H., & Campos, J. (2012). The seismic coupling of subduction zones revisited. *Journal of Geophysical Research*, 117, B05310. <https://doi.org/10.1029/2011JB009003>
- Sclater, J. G., Parsons, B., & Jaupart, C. (1981). Oceans and continents: Similarities and differences in mechanisms of heat loss. *Journal of Geophysical Research*, 86, 11,535–11,552.
- Sibson, R. H. (1973). Interactions between temperature and pore-fluid pressure during earthquake faulting and a mechanism for partial or total stress relief. *Nature Physical Science*, 243(126), 66–68.
- Sibson, R. H. (1975). Generation of pseudotachylyte by ancient seismic faulting. *Geophysical Journal of the Royal Astronomical Society*, 43(3), 775–794.
- Spinelli, G. A., & Harris, R. N. (2011). Thermal effects of hydrothermal circulation and seamount subduction: Temperatures in the Nankai Trough Seismogenic Zone Experiment transect, Japan. *Geochemistry, Geophysics, Geosystem*, 12, Q0AD21. <https://doi.org/10.1029/2011GC003727>
- Spinelli, G. A., & Wang, K. (2009). Links between fluid circulation, temperature, and metamorphism in subducting slabs. *Geophysical Research Letters*, 36, L13302. <https://doi.org/10.1029/2009GL038706>
- Stein, S., & Okal, E. A. (2007). Ultralong period seismic study of the December 2004 Indian Ocean earthquake and implications for regional tectonics and the subduction process. *Bulletin of the Seismological Society of America*, 97, S279–S295.
- Stein, S., & Okal, E. A. (2011). The Size of the 2011 Tohoku earthquake need not have been a surprise. *Eos, Transactions American Geophysical Union*, 92(27), 227.
- Stein, C. A., & Stein, S. (1992). A model for the global variation in oceanic depth and heat flow with lithospheric age. *Nature*, 359, 123–129.
- Stein, C. A., & Stein, S. (1994). Constraints on hydrothermal heat flux through the oceanic lithosphere from global heat flow. *Journal of Geophysical Research*, 99(B2), 3081–3095.
- Suarez, G., & Sánchez, O. (1996). Shallow depth of seismogenic coupling in southern Mexico: Implications for the maximum size of earthquakes in the subduction zone. *Physics of the Earth and Planetary Interiors*, 93, 53–61.
- Suppe, J. (2007). Absolute fault and crustal strength from wedge tapers. *Geology*, 35(12), 1127–1130.
- Syracuse, E. M., Keken, P. E. V., & Abers, G. A. (2010). The global range of subduction zone thermal models. *Physics of the Earth and Planetary Interiors*, 183, 73–90.
- Tanaka, H., Chen, W. M., Wang, C. Y., Ma, K. F., Urata, N., Mori, J., & Ando, M. (2006). Frictional heat from faulting of the 1999 Chi-Chi, Taiwan earthquake. *Geophysical Research Letters*, 33, L16316. <https://doi.org/10.1029/2006GL026673>
- Tichelaar, B. W., & Ruff, L. (1993). Depth of seismic coupling along subduction zones. *Journal of Geophysical Research*, 98, 2107–2037.
- Turcotte, D. L., & Schubert, G. (1973). Frictional heating of descending lithosphere. *Journal of Geophysical Research*, 78, 5876–5886.
- Von Herzen, R., Ruppel, C., Molnar, P., Nettles, M., Nagihara, S., & Ekström, G. (2001). A constraint on the shear stress at the Pacific-Australian plate boundary from heat flow and seismicity at the Kermadec forearc. *Journal of Geophysical Research*, 106, 6817–6833.
- Wada, I., & Wang, K. (2009). Common depth of slab-mantle decoupling: Reconciling diversity and uniformity of subduction zones. *Geochemistry, Geophysics, Geosystems*, 10, Q10009. <https://doi.org/10.1029/2009GC002570>
- Wallace, L. M., Reyners, M., Cochran, U., Bannister, S., Barnes, P. M., Berryman, K., et al. (2009). Characterizing the seismogenic zone of a major plate boundary subduction thrust: Hikurangi margin, New Zealand. *Geochemistry, Geophysics, Geosystems*, 10, Q10006. <https://doi.org/10.1029/2009GC002610>
- Wang, K., & Bilek, S. L. (2011). Do subducting seamounts generate or stop large earthquakes? *Geology*, 39, 819–822.
- Wang, K., & Bilek, S. L. (2014). Fault creep caused by subduction of rough seafloor relief. *Tectonophysics*, 610, 1–24.
- Wang, K., & Dixon, T. (2004). “Coupling” semantics and science in earth research. *Eos, Transactions American Geophysical Union*, 85(18), 180.

- Wang, K., Hyndman, R., & Yamano, M. (1995). Thermal regime of the Southwest Japan subduction zone: Effects of age history of the subducting plate. *Tectonophysics*, 248, 53–69.
- Wang, K., Mulder, T., Rogers, G., & Hyndman, R. (1995). Case for very low coupling stress on the Cascadia subduction fault. *Journal of Geophysical Research*, 100, 12,907–12,918.
- Webb, T. H., & Anderson, H. (1998). Focal mechanisms of large earthquakes in the North Island of New Zealand: Slip partitioning at an oblique active margin. *Geophysical Journal International*, 134, 40–86.
- Wech, A. G., & Creager, K. C. (2011). A continuum of stress, strength and slip in the Cascadia subduction zone. *Nature GeoScience*, 4, 624–628.
- Wells, D., & Coppersmith, K. (1994). New empirical relationships among magnitude, rupture length, rupture width, rupture area, and surface displacement. *Bulletin of the Seismological Society of America*, 84, 974–1002.
- Wessel, P., & Smith, W. H. F. (2013). Generic mapping tools: Improved version released. *EOS. Transactions of the American Geophysical Union*, 94, 409–410.
- Whittington, A. G., Hofmeister, A. M., & Nabelek, P. I. (2009). Temperature-dependent thermal diffusivity of the Earth's crust and implications for magmatism. *Nature*, 458, 319–321.
- Williams, C. A., Eberhart-Phillips, D., Bannister, S., Barker, D. H. N., Henrys, S., Reyners, M., & Sutherland, R. (2013). Revised interface geometry for the Hikurangi subduction zone, New Zealand. *Seismological Research Letters*, 84, 1066–1073.
- Wilson, D. S. (1993). Confidence intervals for motion and deformation of the Juan de Fuca Plate. *Journal of Geophysical Research*, 98(B9), 16,053–16,071.
- Wilson, D. (2002). The Juan de Fuca plate and slab: Isochron structure and Cenozoic plate motions. In S. Kirby, K. Wang, & S. Dunlop (Eds.), *The Cascadia subduction zone and related subduction systems*. US Geological Survey: U.S. Geological Survey Open-File Report 02–328 and Geological Survey of Canada Open File 4350.
- Wolery, T. J., & Sleep, N. H. (1976). Hydrothermal circulation and geochemical flux at mid-ocean ridges. *The Journal of Geology*, 84(3), 249–275.
- Xu, Y., Shankland, T. J., Linhardt, S., Rubie, D. C., Langenhorst, F., & Klasinski, K. (2004). Thermal diffusivity and conductivity of olivine, wadsleyite and ringwoodite to 20 GPa and 1373 K. *Physics of the Earth and Planetary Interiors*, 143–144, 321–336.
- Ye, L., Lay, T., Kanamori, H., & Rivera, L. (2016). Rupture characteristics of major and great ($M_w \geq 7.0$) megathrust earthquakes from 1990 to 2015: 1. Source parameter scaling relationships. *Journal of Geophysical Research: Solid Earth*, 121, 826–844. <https://doi.org/10.1002/2015JB012426>
- Yokota, Y., & Koketsu, K. (2015). A very long-term transient event preceding the 2011 Tohoku earthquake. *Nature Communications*, 6. <https://doi.org/10.1038/ncomms6934>
- Yoshioka, S., Suminokura, Y., Matsumoto, T., & Nakajima, J. (2013). Two-dimensional thermal modeling of subduction of the Philippine Sea plate beneath southwest Japan. *Tectonophysics*, 608, 1094–1108.